

國立交通大學

電子物理系

博士論文

液態鎵的結構、動力學及熱力學性質之研究

Researches on structure, dynamics and thermodynamic properties
of liquid Ga



研究生：蔡昆憲

指導教授：吳天鳴 教授

楊宗哲 教授

中華民國九十七年七月

液態鎔的結構、動力學及熱力學性質之研究

Researches on structure, dynamics and thermodynamic properties
of liquid Ga

研究生：蔡昆憲

Student : Kun-Hsine Tsai

指導教授：吳天鳴 教授

Advisor : Dr. Ten-Ming Wu

楊宗哲 教授

Advisor : Dr. Tzong-Jer Yang



Submitted to Department of Electrophysics

College of Science

National Chiao Tung University

in partial Fulfillment of the Requirements

for the Degree of

Doctor of Philosophy

in

Electrophysics

June 2008

Hsinchu, Taiwan

中華民國九十七年七月

液態鎵的結構、動力學及熱力學性質之研究

學生：蔡昆憲

指導教授：吳天鳴教授

楊宗哲教授

國立交通大學電子物理學系 博士班

摘要

在本論文中，我們將以 molecular dynamics (MD) 作為模擬的方法，以一具有排斥核 (repulsive core) 和 Friedel 震盪 (oscillation) 項所組成的液態鎵 pseudo-potential 作為模擬系統的作用位能，來探討真實液態鎵微觀尺度下的結構、動力學行為及其熱力學特性。於此，我們將這些動力學行為和熱力學特性分成兩部分各自討論。

一、經由非彈性 X-ray 散射 (IXS) 和非彈性中子散射 (INS) 實驗，發現液態鎵的靜態結構因子 (static structure factor) $S(q)$ 有一突起結構，動態結構因子 (dynamic structure factor) $S(q, \omega)$ 的頻譜寬 (line-width) 函數 $Z(q)$ 有一平台結構。這兩異常結構的成因及其物理原理是近年來熱門的話題。故為了解其物理原理，我們以上述所提的液態鎵模型作為系統之作用位能，由粒子流動之

縱向分量相干函數頻譜 (longitudinal current spectra) $C_L(q, \omega)$ 所估計出的系統聲速，和經由計算所得到的動態結構因子幾乎和實驗值吻合。這證明我們所使用的液態鎂模型足以取代真實液態鎂。同時，在我們的模擬系統發現，靜態結構因子 $S(q)$ 中的凸起結構與頻譜寬函數 $Z(q)$ 中的平台結構都約略發生在相同處，但在 $S(q)$ 中凸起結構的產生，需有效位能範圍含蓋到第三個震盪位能井， $Z(q)$ 中平台結構的產生，需有效位能範圍卻只需要含蓋到第二個震盪位能井。

二、 Mansoori-Canfield / Rasaiah-Stell 提出以硬球為基本要件的 MCRS 微擾理論，不但無需沉重的計算且能經濟地幫模型系統找到一有效粒子尺度。再加入 Mon 的修正項，推廣為 Extend-MCRS 微擾理論。此理論更能精確地估計模擬系統的有效粒子尺度和其熱力學性質。利用具有和真實液態鎂相似物理特性的液態鎂模型作為模擬系統的作用位能，除了前章節在此液態鎂模型發現的奇異結構外，其徑向分布函數 (radial distribution function) 的峰值隨密度變化曲線有一不連續跳躍。此外，額外的熵值 (excess entropy) 隨著密度增加而減少，但在某段密度區間內額外的熵值卻不正常增加。此奇異行為可以由系統的粒子最密堆積 (packing fraction) 在此區間內隨密度增加而減少獲得解釋。


Researches on structure, dynamics and thermodynamic properties of the liquid Ga

Student : Kun-Hsine Tsai

Advisors : Professor Ten-Ming Wu
Professor Tzong-Jer Yang

Department of Electrophysics
National Chiao Tung University

Abstract

The logo of National Chiao Tung University is a circular emblem with a gear-like border. Inside the circle, there is a stylized building with the letters 'ES' on it, and a banner at the bottom with the year '1896'.

In this thesis, to investigate the structures, dynamic behavior, and thermodynamic properties of liquid gallium, we use molecular dynamics (MD) method with a liquid gallium pseudo-potential, which consists of a repulsive core and a Friedel-oscillation tail. The discussions for the dynamic behavior and thermodynamic properties of liquid gallium will be separated into two chapters.

According to inelastic neutron scattering (INS) and inelastic x-ray scattering (IXS) experiments, A shoulder appears on the static structure factor $S(q)$ and a dynamic anomaly appears on the linewidth function $Z(q)$ of dynamic structure factor $S(q, \omega)$. The causes of these two anomalous

structures are popular issues in recent decade. In order to investigate the physical origins of these two anomalies, the interatomic pair potential, described above will be the simulated model. The sound velocity of our model which is estimated from longitudinal current spectra $C_L(q,\omega)$ and the dynamic structure factors $S(q,\omega)$ of our model agree well with the experimental results. Therefore, it suggests that the simulated model is good for describing realistic liquid gallium. On the other hand, we report the shoulder of the $S(q)$ and the dynamic anomaly of the $Z(q)$ roughly locate at the some position. The contribution of interaction range of interatomic pair potential to cause the shoulder of $S(q)$ should include the first three attractive wells, but the contribution of interaction range of interatomic pair potential to cause the dynamic anomaly of $Z(q)$ should include the first two attractive wells only.

Mansoori-Canfield / Rasaiah-Stell (MCRS) theory, which is based on hard sphere perturbation theory, can estimate effective diameter of particle efficiently without heavy computing time. By adding a correction term originally proposed by Mon to remedy the deficiency of the MCRS theory, the extended-MCRS theory can accurately predict the effective diameter and thermodynamic properties of simulated system. By using MD simulation with interatomic pair potential given above, there is a discontinuous jump on the

main-peak position of the radial distribution function $g(r)$ at some critical density. Moreover, an anomaly of excess entropy is found to be associated with the anomalous packing fraction η of the hard sphere (HS) fluid in the almost same density region.



誌謝

碩、博士班生涯共七年，這七年，如人飲水、冷暖自知。在此非常感謝我的指導教授 吳天鳴博士，在我研究生生涯的辛苦及不吝指導，因為您要求我必需以嚴格與謹慎的態度面對學問與研究，而讓我覺得博士學位拿的倍感紮實，也是您，帶領我進入科學的殿堂，讓我看到這世界是如此之遼闊，希望之後能繼續保持對學問的嚴謹態度來拓展我未來的研究生涯。

世良學長、柏翰，感謝你們在程式上的指教，生涯規劃的意見，很喜歡學長說的一句話，「我們三個是有革命感情的」。

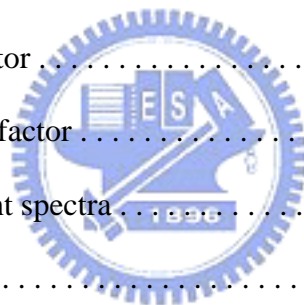
文絢學姊、邦杰、宗哲、葛大哥、光胤、家銘、平翰、小柯、胖子，因為有你們的陪伴，讓博士班研究室顯的更加有朝氣與書卷氣。

一直在背後默默支持我的家人，麗玉阿姨，您就像另一個母親照顧著我和我們家，親愛的妹妹婷婷，鼎煌，乖巧的凱翔因為有你們的加入，讓家裡更顯熱鬧，最後，僅將此論文獻給我敬愛的外公、母親和我摯愛的雅閑、詠亘。

2008.07.30 新竹交通大學

Contents

I Introduction	1
II Anomalies in structure and dynamics of liquid Ga	7
II.1 Introduction	7
II.2 Method	10
II.2.1 Simulated model and molecule dynamics simulation	10
II.2.2 Interatomic pair potentials truncated at different distances	12
II.3 Theory	12
II.3.1 The static structure factor	12
II.3.2 The dynamic structure factor	13
II.3.3 The longitudinal current spectra	14
II.4 Results	15
II.5 Conclusions	35
III Hard sphere perturbation theory for liquid Ga	38
III.1 Introduction	38
III.2 Theory	40
III.2.1 The background of E-MCRS theory	40
III.2.2 Thermodynamic Properties	44
III.3 Model and Method	46
III.3.1 Model	46
III.3.2 Method	48



III.4 Results	49
III.5 Conclusions	61
IV Conclusions	64
V Appendix	67
V.1 WCA Theory	67
V.2 Lado-WCA Theory	73



Chapter I

Introduction

Polyvalent metals (lead, aluminum, gallium, bismuth, etc.) have more strange physical behaviors than alkali metals (lithium, sodium, potassium, rubidium, etc.). Among the polyvalent metals, gallium, exhibiting peculiar structure and electronic properties, has the largest ion number density among the metals belonging to IIB, IIIA, and IVA group: namely, $n_i = 0.051\text{\AA}^{-3}$; further, the electronic density of states (DOS) in liquid gallium shows anomalies associated with some covalent residues. In addition, the liquid phase of gallium is characterized by an electron density of states approaching that of a nearly-free-electron system, which makes it a good candidate for exploiting the simple model of liquid metal dynamics based on the electron-gas-screened ion-ion interaction. Therefore, this thesis emphasizes the important investigations for many physical properties of liquid gallium at temperature close to the melting point $T_m = 303K$.

The nature of microscopic dynamics in alkali and polyvalent metals is nowadays one of the the most lively debated topics in the condensed matter physics. Beyond the truly

hydrodynamic region, the microscopic dynamics, characterized by the occurrence of collective excitations, has attracted many experimentalists in the three decades. Also, the microscopic dynamics can exhibit a dispersion relation extending over a relatively wide range of momentum transfers (typically, up to half the position of the first maximum of the static structure factor). Therefore, several studies performed through inelastic neutron scattering (INS) revealed the presence of a Rayleigh peak and two Brillouin peaks in the dynamic structure factor of many monatomic liquids [1, 2, 3]. The advent of the new radiation sources has allowed the full development of the inelastic x-ray scattering (IXS) [4]. The IXS technique, only related to the coherent dynamics, allows to investigate the collective excitations in the low exchanged momentum (q) region, which is inaccessible by INS. Indeed, liquid alkali metals (liquid rubidium [1, 5], lithium [6], sodium [7], potassium [8], and cesium [9]) and complex liquid metals (mercury [3], aluminum [10], and gallium [11, 12, 13]) have been studied by INS and IXS experiments recently.

On the simulation side, most of liquid metals exhibit the characteristic structural and dynamical features that can be interpreted by the Lennard-Jones potential or the pseudopotential of simple metals [14, 15]. The pseudopotential concept, which is besides offering a deeper comprehension of physical properties such as electrical resistivity, provides a clue for realistic numerical simulation. The numerical simulation framework is particularly useful since the single-particle and the collective dynamics can easily be investigated within technical restrictions due to the finite box size (defining the minimum accessible wave vector) and computation time (related to the statistical quality and to the

energy resolution of the calculated spectra). Broadly speaking, the features of the atomic collective motion, ie., the details of the dynamic structure factor line shape, as an outcome of the molecular-dynamics run, turns out to be less noisy and more straightforward than the corresponding INS results: no absolute normalization is required, no mixing between coherent and incoherent dynamics occurs. Also, the collective dynamics of liquid alkali and polyvalent metals exhibit several features which make these systems candidates to test different theories for the collective dynamics in the liquid state. For example, the generalized kinetic theory predicts that the dominant damping mechanism is provided by a fast process which is thought to be associated with the interactions between an atom and the "cage", its nearest neighbors, in the liquid. By molecular dynamics (MD) simulation, many numerical studies have been reported on alkali and polyvalent metals such as lithium [16, 17], sodium [18, 19], potassium [18, 19], rubidium [18, 19], cesium [18, 19], and liquid gallium [12, 13].

In the first work of this thesis, by simulating a single interatomic pair potential, which consists of a ledge-shape repulsive core and the long-range Friedel oscillations induced by the conduction electrons, the well-known shoulder in the static structure factor and the recently observed anomaly in the linewidth of dynamic structure factor of liquid gallium are reproduced. In our simulations, the two anomalies occur at the same location, which is close to the wavenumber of Friedel oscillations. Both variations of the liquid structure and the linewidth of dynamic structure factor with the different interaction range of the pair potential are also examined. Our results show that the effective range of the pair

potential contributing considerably to the dynamic anomaly should include the repulsive core and the first two attractive wells in the Friedel oscillations, but the effective range for the shoulder structure should be extended up to the first three attractive well. We interpret the occurrence of the dynamic anomaly by a cage-diffusion picture, in which the rigidity of the cage around each ion is enhanced by the coherent attractions between the density waves of ions and the conduction electrons with the wavenumber of Friedel oscillations.

On the other hand, the present status of the theoretical approximation for liquid-structure calculations has a prosperous development in recent three decades. In past two decades, the hypernetted-chain and integral-equation methods were popular for demonstrating structures of alkali and polyvalent metals, which include cadmium ,zinc [20], sodium, potassium, rubidium, cesium [21, 22, 23], germanium, aluminum, lead [23, 24], beryllium, magnesium, calcium, barium [25, 21, 23], and gallium [21]. However, the calculation of the free energy for dense fluids by the hypernetted-chain or integral equation method is nontrivial and tedious.

On the other hand, the structure of some liquid alkali metals (lithium, sodium, potassium, rubidium, and cesium) [26] are studied and compared by thermodynamic perturbations. Besides predicting the structure of liquid metals, thermodynamic perturbation offers a method for predicting the thermodynamic properties of fluids. Although perturbative predictions are not expected to rival those of advanced integral equation or large scale computer simulation method, they are far more numerically efficient than the computer

simulation approaches and often produce comparably accurate results. A key advantage of perturbative approximations is that the structure of fluid is explicitly retained and thus thermodynamic properties can be accurately predicted.

In recent years, many perturbation theories of the thermodynamic properties for fluids have been proposed. The basic principle of these perturbation theories is that the properties of a model system of interest can be obtained in terms of a closely related reference system, for which much is known or can be easily calculated [27]. The "closeness" of the reference and model fluids permits the model fluid free energy to be treated as a perturbation on the reference free energy [28]. Therefore, the hard-sphere fluid should be the excellent candidate for a natural reference fluid because the free energy of the hard sphere reference system is available analytically as fits to accurate machine calculation [29] and the analytic pair distribution function obtained from the Percus-Yevick equation [30]. According to these convenient conditions of the hard-sphere fluids, the extensive applications of hard sphere perturbation theory (HSPT) are over many decades for a wide range of liquid [31]. In the literature review of HSPT [27, 28, 31, 32, 33, 34, 35, 36, 37], although the HSPT is already a complete theory for thermodynamic property and has played an important pioneering role in the study simple liquid, there are few researches about polyvalent metals with HSPT, especially, liquid gallium.

In the second work of this thesis, we report the study of the thermodynamic properties of liquid gallium ($T=323\text{K}$) by HSPT, because there is no investigation or literature related to this work so far. By investigating the thermodynamic properties of a liquid-gallium

model close to the triple point, we have extended the application of the hard sphere perturbation theory (HSPT) to an interatomic pair potential, which has a ledge-shape repulsive core and the long-range oscillations. The structure of this model is interesting for a discontinuity in the density variation of the main-peak position of the radial distribution function. The validity of a HSPT for this model fluid at high densities is essentially determined by the discontinuity on the effective HS diameter estimated by the theory. A correction to remedy the inherent deficiency of the HSPT is proposed by Mon. The new perturbation theory is found to be superior to other first-order HSPT in predicting the thermodynamic properties of the model fluid, including an anomaly in the excess entropy.



Chapter II

Anomalies in structure and dynamics of liquid Ga

II.1 Introduction

The properties of collective dynamics in liquid metals have been studied by the inelastic neutron scattering (INS) and inelastic X-ray scattering (IXS) technique for a long time. Although some physical properties can be obtained by hydrodynamic theory, most of peculiar features in the excitation spectra of polyvalent liquid metals can not be described by this theory [38]. Therefore, to investigate the collective properties in the hydrodynamic regime and collective dynamics in the kinetic regime of these liquid metals is an interesting and important subject. As the wavelengths of the collective dynamics are smaller than the average interparticle distance in these liquids, the propagating sound mode is strongly damped and dynamic structure factor has only a single Lorentzian-like central peak [39].

According to Waseda's classification [40], liquid Ga is one of the polyvalent liquid metals with anomalous structure. The anomalous structure, characterized by a shoulder

on the high-wavevector side of the first peak of the static structure factor $S(q)$, can not be interpreted by a hard-sphere (HS) model. In the pseudo-potential theory, the interatomic pair potential of a polyvalent liquid metal generally has a ledge-shape repulsive core and the long-range Friedel oscillations induced by the conduction electrons [41]. The appearance of the shoulder in a $S(q)$ of the polyvalent liquid metals (gallium, silicon, germanium, tin and bismuth) [41, 42, 43, 44] is associated with the "ledge-shape" repulsive core of the interatomic pair potential, which is obtained from the optimized random phase approximation. Mon [45] shows that the shoulder of the $S(q)$ in liquid gallium is also reproduced by using an interatomic pair potential with a subsidiary minimum at a relative short distance, which is induced by the dynamically screened fluctuating dipole interactions between ion cores. These results [41, 42, 43, 44, 45] indicate that the occurrence of the shoulder in $S(q)$ is strongly dependent on the short-range (ledge-shape) repulsive core of the interatomic pair potential, and these results are concluded with two characteristic length scales: the effective diameter of the repulsive core and the wavelength λ_F of the Friedel oscillations, and the shoulder is expected to occur near $2k_F$, where $k_F = \pi/\lambda_F$ is the magnitude of Fermi wavevector of the conduction electrons [44].

Recently, an anomaly on the high-wavevector side of the de Gennes narrowing [46] in the linewidth $Z(q)$ of dynamic structure factor $S(q, \omega)$ of liquid gallium close to the melting point (303K) is observed by the measurements of IXS [47] and quasielastic neutron scattering (QENS) [48]. The linewidth $Z(q)$ as a function of wavevector q of the collective dynamics shows a minimum, known as de Gennes narrowing, occurring near q_M , the first

peak of the $S(q)$ of the liquid [46]. This anomaly, whose position is coincident with that of the shoulder in $S(q)$ [47, 48], is similar as the one observed by the inelastic neutron scattering (INS) method [49] for liquid bismuth; further, another evidence of the anomaly in linewidth $Z(q)$ is provided by an experiment of liquid germanium by QENS [50]. Thus, the anomaly occurring in $Z(q)$ is expected to be a common feature to those polyvalent liquid metals exhibiting a peculiar shoulder in the $S(q)$ [51, 52, 53, 54, 55]. Theoretically, in classical molecular dynamics (MD) simulation, the calculation of the static and dynamic structure factor can be done for larger simulation systems than that of *ab initio* simulation system. In the kinetic theory, the linewidth $Z(q)$ can be described by the revised Enskog theory for the HS fluids, generalized by including the correlated collisions among particles [56].

It is interesting to understand the correlation between the shoulder in $S(q)$ and the anomaly in the $Z(q)$ of dynamic structure factor. We use MD simulation with an interatomic pair potential, generated from the first-principles generalized energy independent nonlocal model-pseudopotential (GEINMP) theory [57], and we successfully reproduce the anomalies in $S(q)$ and $Z(q)$. These results agree well with the experimental data of liquid gallium [58]. To study the correlation of the shoulder and the anomaly and to examine the contribution of effective range of the interatomic pair potential for both shoulder and anomaly are a primary theme in this chapter. Finally, we give a physical explanation for the occurrence of the anomalies in the static structure factor $S(q)$ and in the linewidth $Z(q)$ of dynamic structure factor.

II.2 Method

II.2.1 Simulated model and molecule dynamics simulation

Using MD simulation with interatomic pair potential generated from the GEINMP theory [57], we have carried out the NVT ensemble with 3500 particles in the equilibrium state of liquid Ga at $T = 323K$, pressure about 1 bar and number density $\rho = 0.05\text{\AA}^{-3}$ [59]. In the simulation, the particles are confined in a cubic box of length 41.23\AA and the periodic boundary conditions are used. The interatomic pair potential $\phi(r)$ is shown in Fig. II.1, and have two parameters: $\sigma = 4.04\text{\AA}$, the shortest distance where the potential is zero, and ε , the depth of the first attractive well, corresponding to an effective temperature about $47K$. The pure repulsive core of $\phi(r)$ is the range inside the minimum of the first attractive well, which occurs at $\sigma_0 = 1.07\sigma$. The repulsive core, which is much softer than that of the LJ potential, has a ledge shape with a curvature change around 0.8σ [60]. Beyond σ_0 , $\phi(r)$ has an oscillatory part, which is the so-called Friedel oscillations with the first, second and third maxima at $\sigma_1 = 1.28\sigma$, $\sigma_2 = 1.77\sigma$ and $\sigma_3 = 2.26\sigma$, respectively. As distance is farther than 3σ , the oscillatory part can be well described by the equation of the shifted Friedel oscillations [41]

$$\phi_{FO}(r) = V \frac{\cos(2k_F r + \alpha)}{(2k_F r)^3}, \quad (\text{II.1})$$

where $k_F = 16.24nm^{-1}$. Hence, the wavelength λ_F of the Friedel oscillations is 1.93\AA and the effective valence per ion in the simulation is estimated to be 2.9.

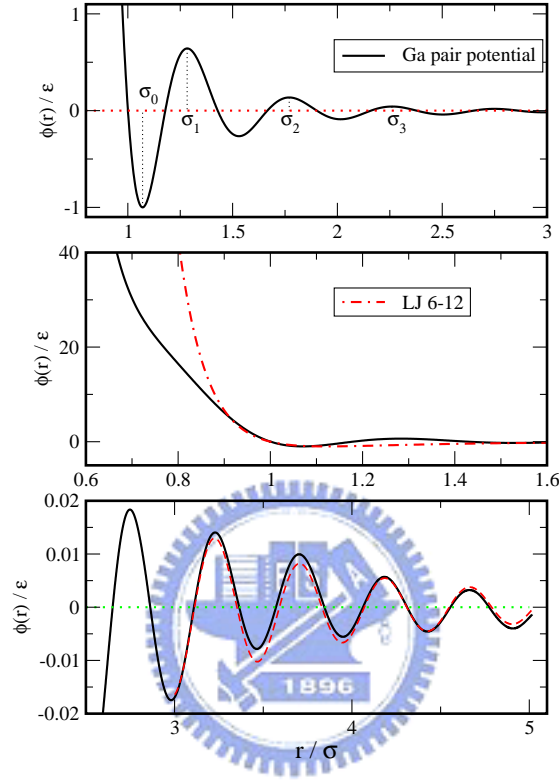


Figure II.1: (a) Interatomic pair potential $\phi(r)$ obtained from the first-principles GEINMP theory for liquid Ga at $T = 323K$ [57]. ε , corresponding to a temperature about $47K$, is the depth of the first attractive well. $\sigma = 4.04\text{\AA}$ is the shortest distance where the pair potential is zero. The first minimum of $\phi(r)$ is located at $\sigma_0 = 1.07\sigma$, the first maximum is at $\sigma_1 = 1.28\sigma$, the second maximum is at $\sigma_2 = 1.77\sigma$, and the third maximum is at $\sigma_3 = 2.26\sigma$. (b) Comparison between $\phi(r)$ (solid line) and the LJ potential (dotted-dashed line) with the same ε and σ . (c) The pair potential $\phi(r)$ at distances larger than 3σ . The dashed line is the fitting result with Eq. II.1.

II.2.2 Interatomic pair potentials truncated at different distances

In order to investigate the effects of the repulsive core and the oscillatory part of $\phi(r)$ on the structures, physical properties, and collective dynamics of the simulated liquid, we perform the same NVT conditions with the pair potential $\phi_i(r)$, for $i = 0, 1, 2, 3$, obtained by truncating $\phi(r)$ at σ_i and shifting in energy with the value $\phi(\sigma_i)$. $\phi_i(r)$ is finite in range with cutoff at σ_i , where $\phi_0(r)$ has only the ledge-shape repulsive core, $\phi_1(r)$ includes the repulsive core and the first attractive well, $\phi_2(r)$ and $\phi_3(r)$ are extended to include the first two and three attractive wells, with the depth of the attractive well decreasing with distance r .

II.3 Theory

II.3.1 The static structure factor



The static structure factor $S(q)$, describing the Fourier components of density fluctuations in a liquid, can be measured by INS or IXS experiments. It is related to radial distribution function through a three-dimensional Fourier transform, and can be presented as

$$S(q) = 1 + 4\pi\rho \int_0^\infty r^2 \frac{\sin(qr)}{qr} g(r) dr, \quad (\text{II.2})$$

where $g(r)$ is the radial distribution function of the liquid. ρ is the density of the liquid and q is the wavevector. As k is large, $S(q)$ approaches to one.

II.3.2 The dynamic structure factor

Probed by INS, the dynamic structure factor $S(q, \omega)$ of a liquid consists of the coherent and incoherent parts, associated with the collective and single-particle dynamics in the liquid [61], respectively. When the scattering wavevectors are larger than q_M , the first peak position of $S(q)$, only the coherent part survives and is referred as QENS [48]. In the IXS, without kinematical restrictions, $S(q, \omega)$ has only the coherent part over the energy range of particle dynamics, which makes this technique suitable for the investigation of collective dynamics in liquids [11]. The advantage of MD simulation is to provide the dynamic and structural information which is not accessible in real experiments. The $S_{MD}(q, \omega)$, presented as

$$S_{MD}(q, \omega) = \frac{1}{2\pi} \int_{-\infty}^{\infty} F(q, t) \exp(i\omega t) dt, \quad (\text{II.3})$$

can be obtained via a time Fourier transform of the intermediate scattering function $F(q, t)$ [39], which is generated directly by MD simulation with an interatomic pair potential.

As the wavevectors are smaller than $q = 12.5 \text{ nm}^{-1}$ one-half of q_M , dynamic structure factor is characterized by a central peak component due to quasi-elastic scattering, and two side components due to inelastic scattering from collective excitations, generally referred as the Brillouin lines. As the wavevectors are larger than q_M , the linewidth of central peak in the $S(q, \omega)$ is caused by the non-propagating heat mode. In the revised Enskog

theory for a HS fluid with diameter σ_{hs} , $Z(q)$ can be expressed as [56, 64, 65]

$$Z_E(q) = \frac{D_E q^2}{S_{hs}(q)} d(q), \quad (\text{II.4})$$

where D_E and $S_{hs}(q)$ are the Enskog diffusion coefficient and the static structure factor of the HS fluid, respectively. $d(q)$, characterizing the cage diffusion in the HS system is a dynamic factor, and can be approximated by $d(q) = (1 - j_0(q\sigma_{hs}) + 2j_2(q\sigma_{hs}))^{-1}$, where $j_n(x)$ is the spherical Bessel function of order n [65]. In this theory, D_E is given by

$$D_E = \frac{\sigma_{hs}}{8} \left(\frac{\pi k_B T}{m} \right)^{1/2} \frac{(1 - \eta)^3}{\eta(2 - \eta)}, \quad (\text{II.5})$$

where m is the mass of particle, k_B is the Boltzmann constant, and $\eta = \pi\rho\sigma_{hs}^3/6$ is the packing fraction. Thus, σ_{hs} is the only parameter to be determined in Eq. II.5.

II.3.3 The longitudinal current spectra

The longitudinal current spectrum is given by

$$C_L(q, \omega) = \frac{1}{2\pi} \int_{-\infty}^{\infty} C_L(q, t) \exp(i\omega t) dt, \quad (\text{II.6})$$

where $C_L(q, t)$, the longitudinal current correlation function, can be shown as

$$C_L(q, t) = \frac{1}{N} \langle j_{\mathbf{q}}^z(t) \cdot j_{-\mathbf{q}}^z(0) \rangle, \quad (\text{II.7})$$

where $j_{\mathbf{q}}^z(t)$ is the component of the current function $\vec{j}_{\mathbf{q}}(t)$ that is parallel to the direction of the wave vector \vec{q} . The current function $\vec{j}_{\mathbf{q}}(t)$ is given by

$$\vec{j}_{\mathbf{q}}(t) = \sum_{l=1}^N \vec{v}_l(t) \cdot \exp[-i\vec{q} \cdot \vec{r}_l(t)], \quad (\text{II.8})$$

where l is the index of particle, and \vec{v} and \vec{r} is the velocity and coordinate of particle, respectively. As can be seen, the $C_L(q, \omega)$, calculated as the Fourier transforms of the $C_L(q, t)$ [39], are in good agreement with those obtained via the equation $C_L(q, \omega) = \omega^2 S(q, \omega)/q^2$. The main peak position of $C_L(q, \omega)$ for each q is used to plot the dispersion curve, and the slope of the dispersion curve is closely related to the sound velocity of the system.

II.4 Results

For $\phi(r)$, the simulated $S(q)$ shows a maximum located at q_M ($25.4nm^{-1}$), and a shoulder appear on the high- q side of the first peak. Shown in Fig. II.2, the shoulder in the simulated $S(q)$ occurs around $32.5nm^{-1}$, which is exactly equal to $2k_F$. Moreover, the first peak and the shoulder of simulated $S(q)$ agree with those of experimental data above the melting temperature [40], although the values of the simulated $S(q)$ at low q deviate from experimental ones.

In order to investigate the relationship between the shoulder in $S(q)$ and the interatomic potential including the repulsive core and Friedel oscillation parts, we examine the variation of the radial distribution functions $g(r)$ and $S(q)$ with the interaction range of the interatomic potential referred to Fig. II.1. First, Fig. II.3 shows the variation of the radial distribution functions $g_i(r)$, compared with $g(r)$ of the full-range $\phi(r)$. The first peak in all radial distribution functions almost locates at 0.686σ , which is inside

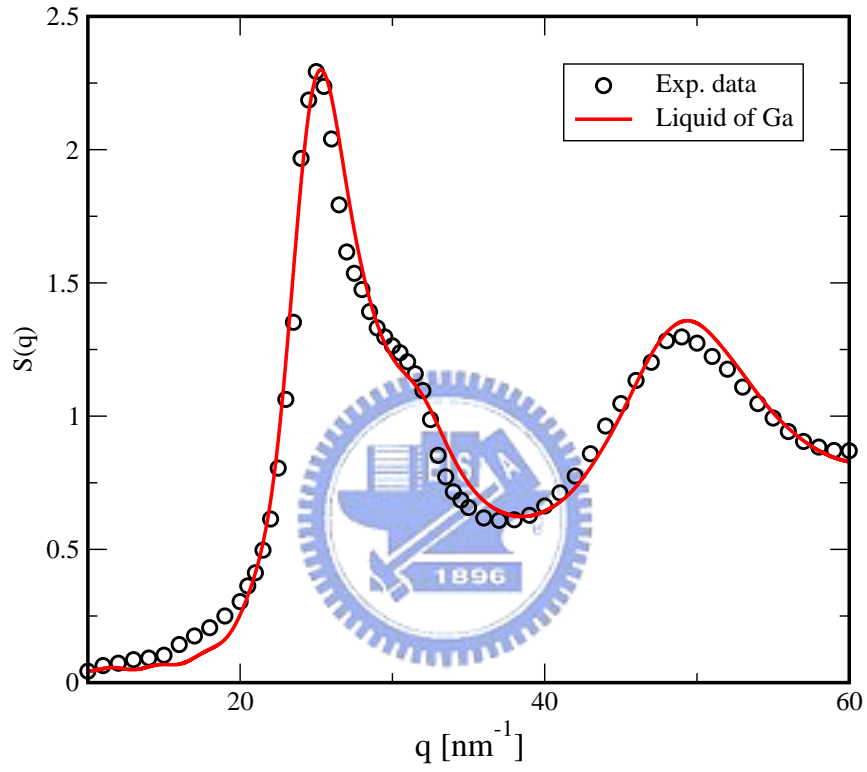


Figure II.2: Comparison of the simulated static structure factor (solid line) with the experimental data of liquid Ga at T=323K (open circles) [40].

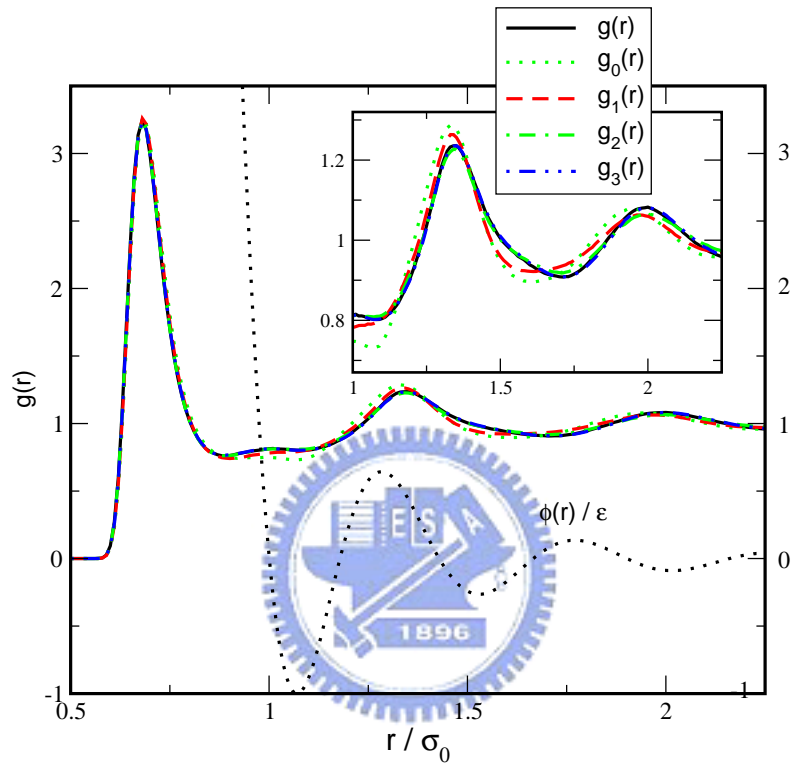


Figure II.3: The radial distribution functions: $g(r)$ (solid line), $g_0(r)$ (dotted line), $g_1(r)$ (dashed line), $g_2(r)$ (dot-dashed line) and $g_3(r)$ (dot-dot-dashed line). $g(r)$ is for the full-range pair potential $\phi(r)$, indicated by the thinner dotted line, and $g_i(r)$ is for the truncated pair potential $\phi_i(r)$. The second and third shells of the radial distribution functions are enlarged in the inset.

the repulsive core, and the shapes of $g_i(r)$ are almost the same, no matter where the interaction distance is truncated. The evident difference is only for tail of radial distribution functions that indicates the Friedel oscillations of the interatomic potential make the second- and third-shell structures of radial distribution function an outward shift, and this shift enhances the values of radial distribution function at distances around the minimum of the Friedel oscillations. The outward shifts of the second and third shells have little reduction by including the first attractive part referred to Fig. II.3. It means that the Friedel oscillations beyond the first attractive part have a certain effect on the structures of the liquid. Extending the interaction range to the third attractive well of the Friedel oscillations, $g_3(r)$ can be completely identical with $g(r)$. The results mildly imply that the shoulder structure may be a result of the interplay between the ledge-shape repulsive core and the Friedel oscillations; however, Matsuda [66] and Canales [67] suggest that the structures of liquid alkali metals are almost identical by considering the repulsive core and the short-range attractive part of interaction potential.

Secondly, the simulated static structure factors $S_i(q)$ with the truncated interatomic potentials $\phi_i(r)$ ($i = 0, 1, 2, 3$) are shown in Fig. II.4, with $S(q)$ as a reference one. The first peak and the shape around $32.5nm^{-1}$ in these static structure factors should be examined particularly. For the $S_0(q)$, no shoulder appears on the high- q side of the first peak, which shifts to $25.7nm^{-1}$ and has an increase in magnitude. The simulated $S_1(q)$ deviates more from a HS fluid than the liquid of pure repulsive core because the first attractive well is included in the interaction range. The first peak of $S_1(q)$ is evident

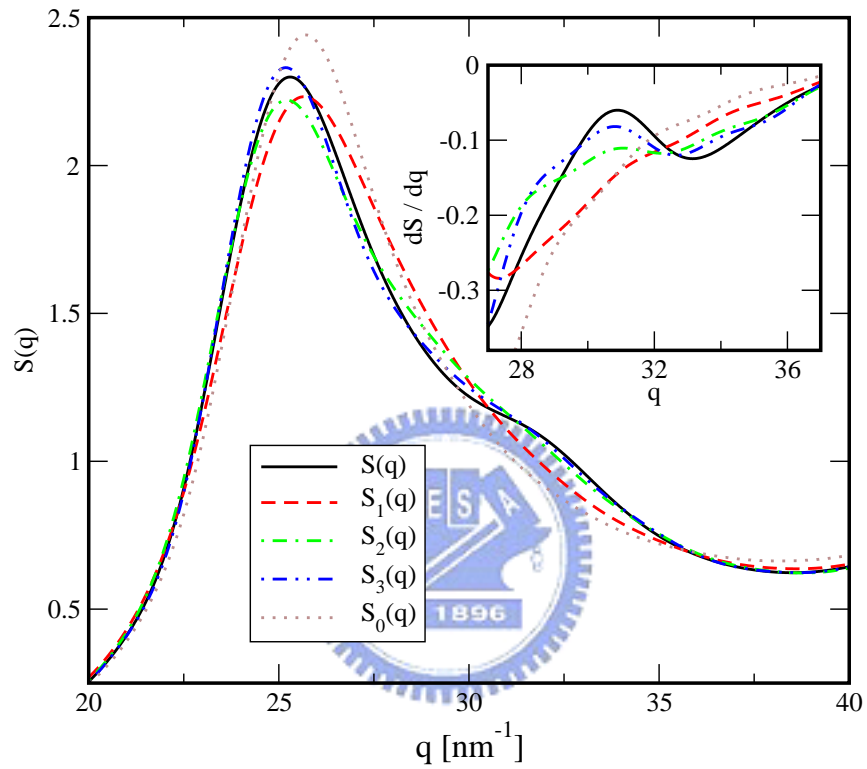


Figure II.4: The static structure factors: $S(q)$ (solid line), $S_0(q)$ (dotted line), $S_1(q)$ (dashed line), $S_2(q)$ (dot-dashed line) and $S_3(q)$ (dot-dot-dashed line). $S(q)$ is for the full-range pair potential $\phi(r)$ and $S_i(q)$ for the truncated pair potential $\phi_i(r)$ ($i = 0, 1, 2, 3$) with a cutoff at σ_i .

to be lower than that of $S_0(q)$, but the position has no significant change; however, the values of $S_1(q)$ for q between $28nm^{-1}$ and $35nm^{-1}$ are elevated. For $S_2(q)$, the position of the first-peak shifts closer to that of $S(q)$, and the magnitudes in the shoulder region continuously increase to get closer to $S(q)$. To extend the interaction range to including the third attractive well of Friedel oscillations, the magnitude of the first peak is almost close to that of $S(q)$, and a complete shoulder appears on the high- q side of the first peak.

Quite sensitive to the behavior of the static structure factor, the appearance of the shoulder structure can be further identified by the derivative of $S_i(q)$ with respect to q , $dS_i(q)/dq$, for q around $32.5nm^{-1}$. In general, on the high- q side of the first peak of $S_i(q)$, $dS_i(q)/dq$ is negative and increases with q . Mathematically, a monotonical increase of $dS_i(q)/dq$ with q indicates no appearance of a shoulder in $S_i(q)$ in the region investigated. However, once a shoulder appears in $S_i(q)$, the behavior of $dS_i(q)/dq$ is distorted to show some extremes, instead of increasing monotonically. Shown in the inset of Fig. II.4 are the numerical results of $dS_i(q)/dq$ for q in the shoulder region. Both $dS_0(q)/dq$ and $dS_1(q)/dq$ increase monotonically, indicating that no shoulder appears on the high- q side of the first peak of $S_0(q)$ or $S_1(q)$. $dS_2(q)/dq$ shows very weak extremes, signaling the emergence of a weak shoulder in $S_2(q)$. Manifested by the clearly observed extremes in $dS_3(q)/dq$, the structures in the liquid simulated with $\phi_3(r)$ are developed well enough to produce a shoulder on the high- q side of the first peak of $S_3(q)$. Our results clearly indicate that the liquid structures are mainly determined by the repulsive core and the long-range Friedel oscillations induced by the conduction electrons, and the effective interaction range must

Pair potential	N_{1201}	N_{1211}	N_{1301}	N_{1311}	N_{1421}	N_{1422}	N_{1431}
$\phi(r)$	0.189	0.045	0.134	0.252	0.042	0.092	0.065
$\phi_0(r)$	0.164	0.047	0.118	0.252	0.050	0.101	0.077
$\phi_1(r)$	0.177	0.046	0.124	0.254	0.047	0.096	0.071
$\phi_2(r)$	0.190	0.046	0.132	0.251	0.042	0.091	0.065
$\phi_3(r)$	0.189	0.045	0.135	0.251	0.042	0.092	0.064

Table II.1: The averaged fractions of atomic bonded pairs, N_{ijkl} [63], in the liquids simulated with the full-range pair potential $\phi(r)$ and the truncated $\phi_i(r)$

include at least the first three attractive wells.

To manifest further the modulation on local structures by Friedel oscillations, we calculate the numbers of atomic bonded pairs (ABPs) [62] in the liquids for the pair potentials at different truncations. In the previous studies, it has been shown numerically that as the system simulated with the pair potential generated by the GEINMP theory is quenched from the liquid phase into the amorphous solids or the β -phase crystal, the 1201-type atomic bounded pairs (ABPs), clusters of four atoms formed by a root pair and two neighboring atoms, become predominated [63]. Also, some large clusters formed by more 1201-type ABPs may produce a high- q shoulder in $S(q)$ [59]. In Table II.1, our calculated results for the APBs show that by truncating the pair potential $\phi(r)$ at σ_0 , the numbers of the 1201- and 1301-type ABPs decrease significantly but those of the 1421-, 1422- and 1431-type increase. With the cutoff at σ_1 , the numbers of those ABPs mentioned above are still different from those of the full-range $\phi(r)$, although the differences are reduced. As the cutoff is extended up to σ_2 , the numbers of the ABPs are almost the same as those

of $\phi(r)$. Thus, our present analysis on the ABPs suggests that the Friedel oscillations within the intermediate region, up to the third attractive wells, cause a modulation on the local structures determined by the repulsive core and such a modulation favors the emergence of some solid-like clusters which cause a shoulder on the high- q side of the first peak in $S(q)$.

To investigate the anomaly in collective dynamics, we have calculated the dynamic structure factor $S_{MD}(q, \omega)$, a time Fourier transform of the intermediate scattering function of Ga interatomic potential. These intermediate scattering functions are obtained by simulations for wavevectors chosen to be the reciprocal lattice points of the simulated box. In order to fit the experimental data, $S_{MD}(q, \omega)$ has to be modified to satisfy the detailed balance condition and convoluted with the instrumental resolution function $R(\omega)$ [11]:

$$I_N^{th}(q, \omega) = \int \frac{\hbar\omega' / KT}{1 - \exp(-\hbar\omega' / KT)} S_{MD}(q, \omega') R(\omega - \omega') d\omega', \quad (\text{II.9})$$

and the calculated dynamics structure factors $I_N^{th}(q, \omega)$ are directly compared with the experimental data of IXS. In hydrodynamic regime, a comparison between the best fitting for selected q and the experimental spectrum is reported in Fig. II.5. Only for $q = 3.25 \text{ nm}^{-1}$, the central peak of $I_N^{th}(q, \omega)$ is disappeared because of the effect of simulated system size; however, the two Brillouin peaks can be fitted well. For several q values in the kinetic regime, from the first peak to the second minimum in $S(q)$, the dynamic structure factors calculated by our simulation are also in good agreement with the experimental

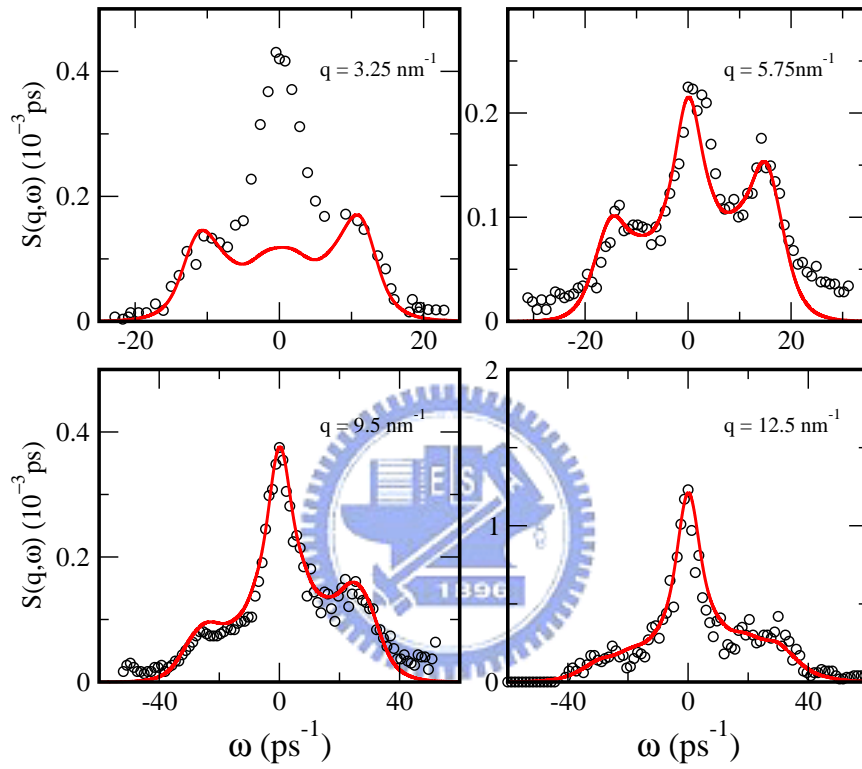


Figure II.5: Dynamic structure factor at the indicated wavevectors. The IXS spectra at 315 K are shown as open circles, and the simulated dynamic structure factors at 323 K are shown as solid lines. The width of the instrument resolution function is about 3.0 meV .

data, and the comparison is reported in Fig. II.6.

Since attention is focused on $S(q, \omega)$, it is more convenient to examine the $C_L(q, \omega)$, which is defined in Eq. II.6. In the same manner as the experimental inelastic x-ray data [68, 69], we analyze the longitudinal current spectra which is fitted by the simple damped harmonic oscillator (DHO) function

$$C_L(q, \omega) = A \frac{\gamma_L \omega}{(\omega^2 - \omega_L^2)^2 + (\gamma_L \omega)^2}, \quad (\text{II.10})$$

where A is a fitting; on the other hand, ω_L and γ_L is energy position shift and width of spectra, respectively. For several q values between $q = 3.25 \text{nm}^{-1}$ and $q = 15.0 \text{nm}^{-1}$, the longitudinal current spectra with the DHO fitting lines are shown in Fig. II.7.

Shown in Fig. II.8, the dominant q dependence of the shift ω_L is linear below $q = 10.0 \text{nm}^{-1}$, which confirms our results with those observation in the inelastic x-ray measurements [11]. The sound velocity of our system is estimated about 2850ms^{-1} , which is slightly lower than the value 3000ms^{-1} observed in the IXS experiment at 315K . However, the estimated value of sound velocity is almost the same as the value (2800ms^{-1}) as deduced by ultrasonic measurements [11]. Also, the interaction range has very little effect on the sound velocity of system because the sound velocity for each simulated interaction potential is around $2850 \pm 20 \text{ms}^{-1}$. Shown in Fig. II.9, the damping factor γ_L/q of neutron data is compared with the data obtained by fitting our MD simulation data (Eq. II.10). The two sets of data are once again in good agreement with each other and both are consistent with that γ_L/q , is approximated to be a q -independent constant between

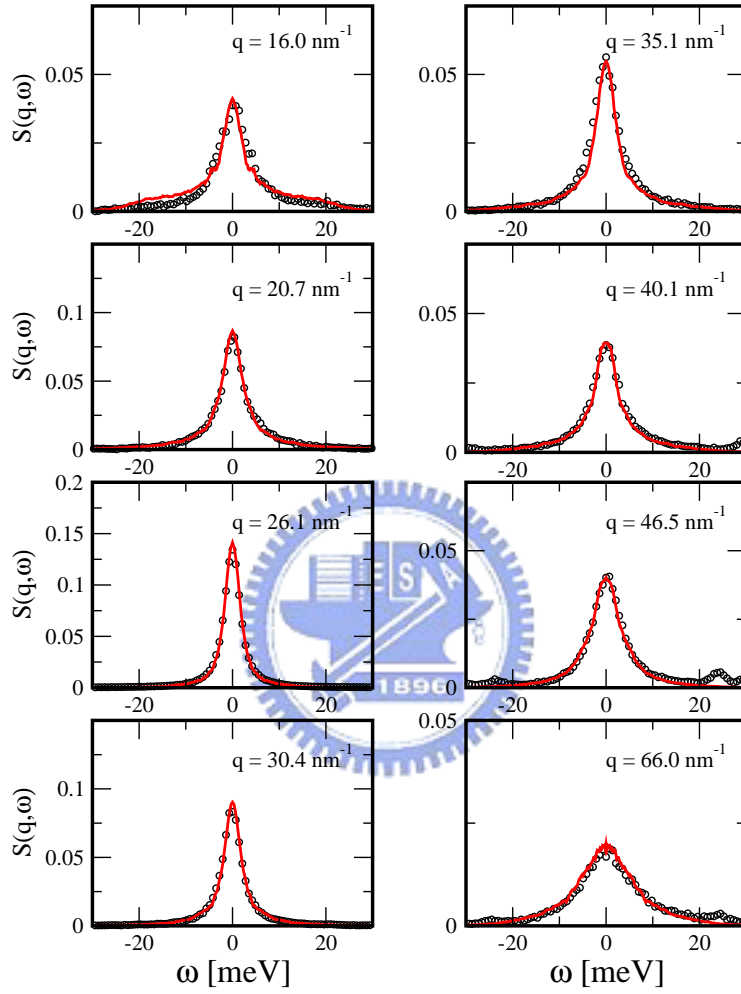


Figure II.6: Comparison between the simulated dynamic structure factors at $T = 323K$ (solid lines) and the IXS experimental data of liquid Ga at $T = 315K$ (circles) [47].

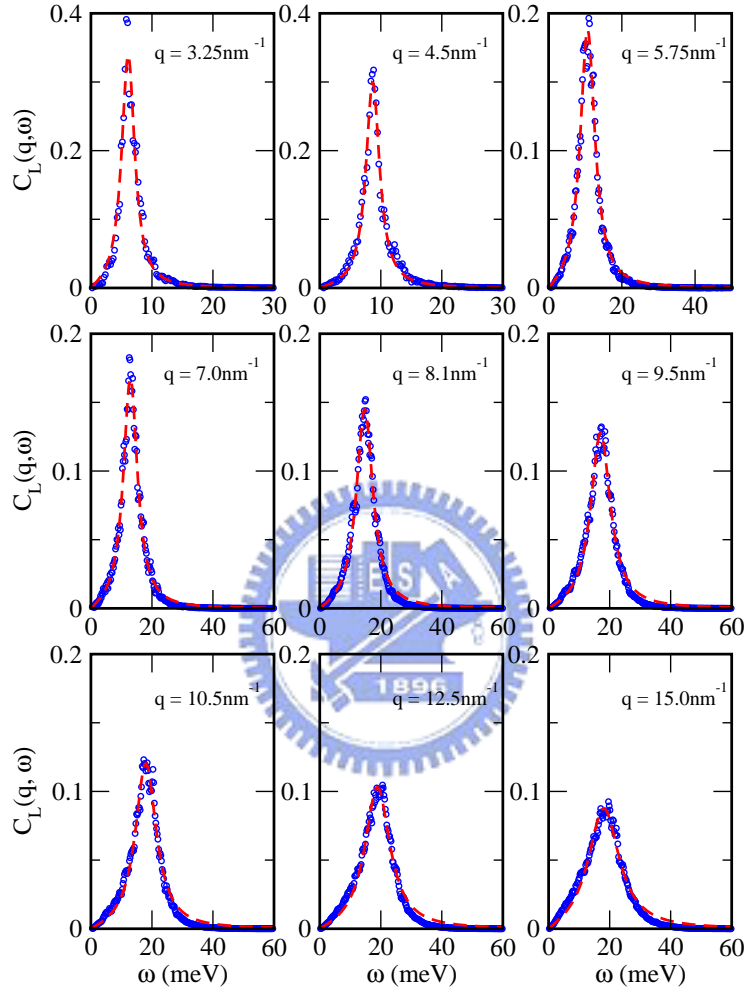


Figure II.7: The simulated longitudinal current spectra at $323K$ (open circles), and the fitting function of the damped harmonic oscillator described in the text (dashed lines).

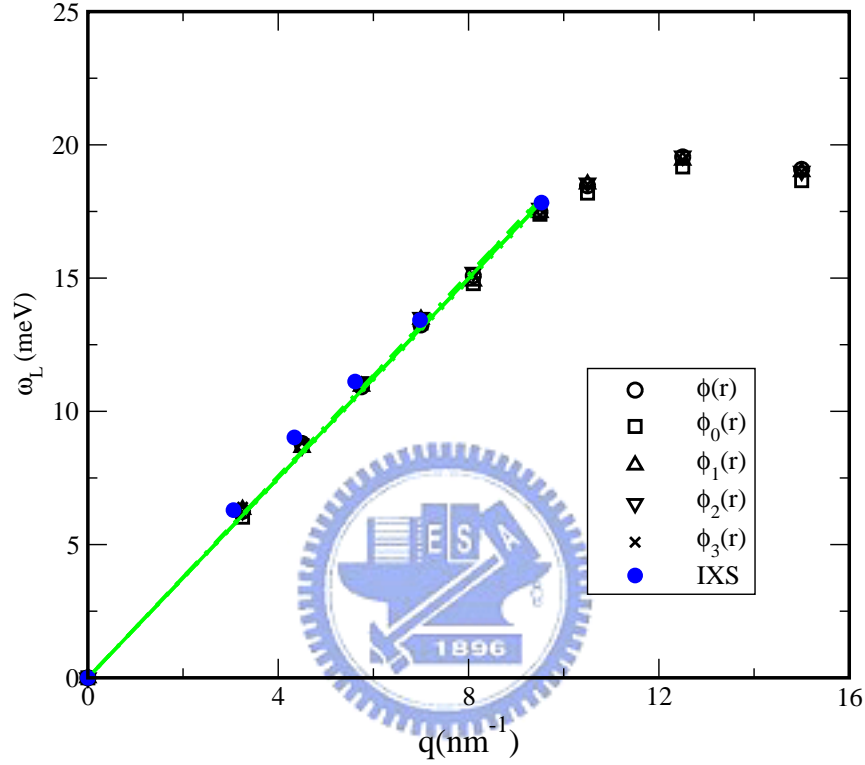


Figure II.8: Dispersion relation obtained by fitting the simulated longitudinal current spectra with damped harmonic oscillator model. The IXS data at 315K from [11] are shown as solid circles. The solid lines are the linear fit to the data of q less than the available data of the IXS experiment. The estimated value of sound velocity for each pair potential is $C_{full} = 2847.3m/s$, $C_{1min} = 2829.7m/s$, $C_{1max} = 2843.4m/s$, $C_{2max} = 2875.6m/s$, and $C_{3max} = 2870.0m/s$, respectively.

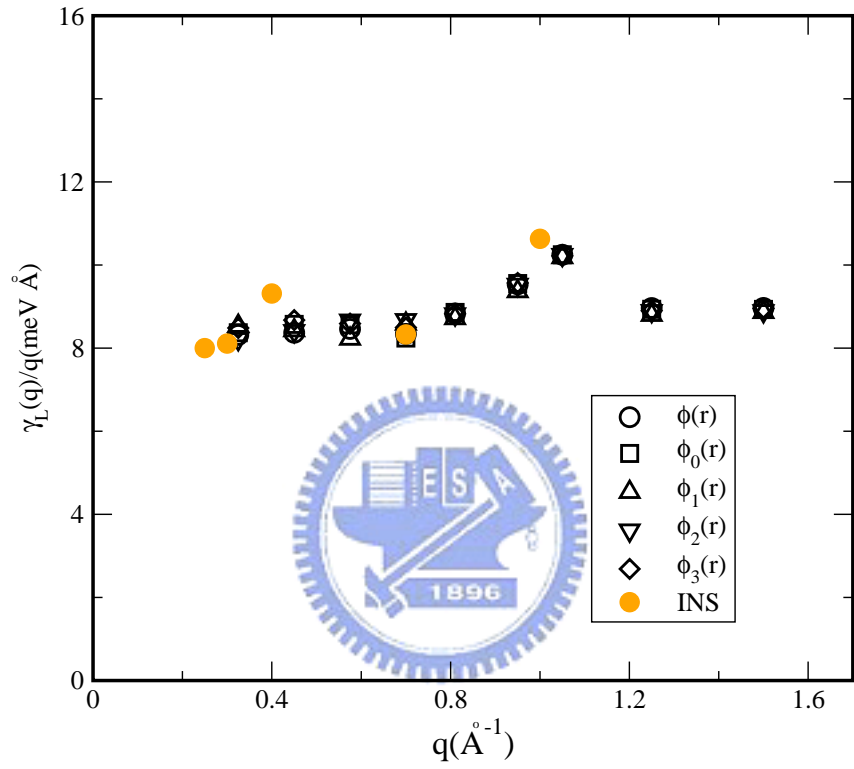


Figure II.9: The damping factor γ_L/q versus q . Neutron data at 315K from [11] are presented as solid circles, and MD simulated data with various interaction range are presented as open symbols.

$q = 0.2nm^{-1}$ and $q = 0.8nm^{-1}$. On the other hand, the γ_L/q values of various interaction ranges are almost the same and that means the interaction range also can not affect the linewidth of longitudinal current spectrum. It is worth pointing out that the relaxation time of the longitudinal current function is linear with the q value in low- q region, but the interaction range of pair potential has no effect on the relaxation time.

As wavevectors larger than $15nm^{-1}$, $S_{MD}(q, \omega)$ can be fitted with a single Lorentzian . We define $Z(q)$ for each q as the half width at half maximum (HWHM) of the Lorentzian. Shown in Fig. II.10, the $Z(q)$ data obtained by our simulations are compared with the experimental data from IXS [47] and QENS [48] technique. The linewidth $Z(q)$ of both experiments and simulation have a minimum, the de Gennes narrowing, which occurs very close to q_M the location of the maximum of $S(q)$. In experiments, an anomaly, which is a shoulder, is observed on the high- q side of the de Gennes narrowing. In our simulation, the linewidth $Z(q)$ agrees well with the general features of both the experimental data, especially the shoulder around $32.5nm^{-1}$. Considering $S(q)$ and $Z(q)$ both generated by our simulations with $\phi(r)$, we confirm that the anomalies in these two functions occur at the same position.

Fig. II.11 shows that both the de Gennes narrowing and the shoulder of the linewidth $Z(q)$ are predicted quite well by the revised Enskog theory, in which σ_{HS} must be the position of the first peak of $g(r)$ (0.686σ) [58] and the reduced density equals $\rho\sigma_0^3 = 3.305$. While the reduced density is equal to 3.305, the packing fraction η is estimated to be 0.558, which is just beyond the fluid-solid boundary of the HS system. Hence, D_E

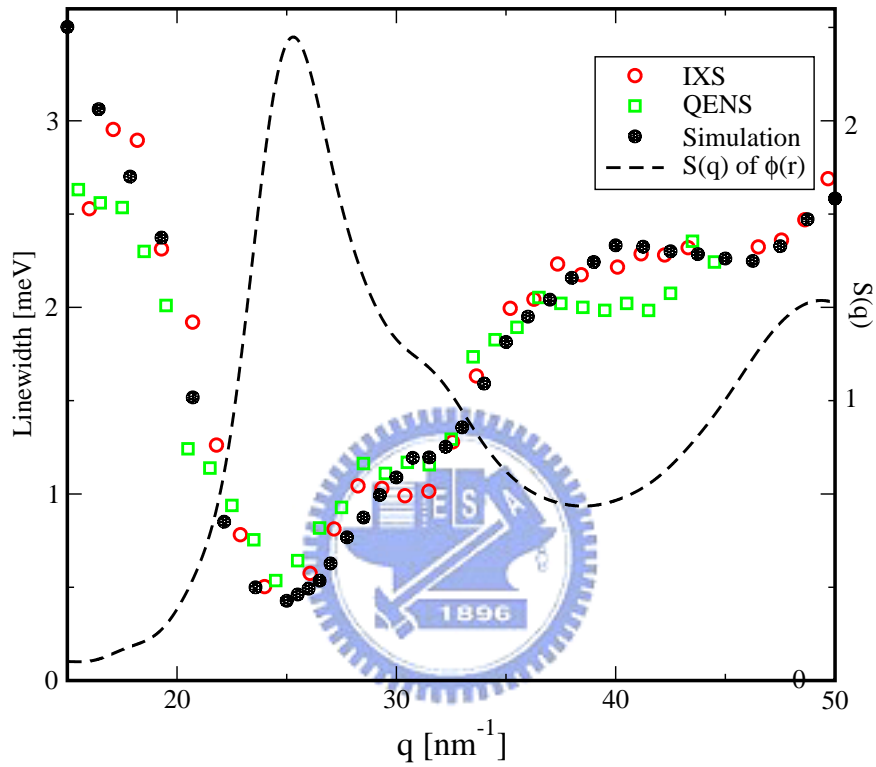


Figure II.10: The spectral linewidth (HWHM) of dynamic structure factors. The open circles and squares are the experimental data of IXS [47] and QENS [48] at $T = 315K$, respectively. The solid circles are the simulated results with $\phi(r)$ at $T = 323K$. The dashed line is the simulated $S(q)$, with a scale referred to the right axis.

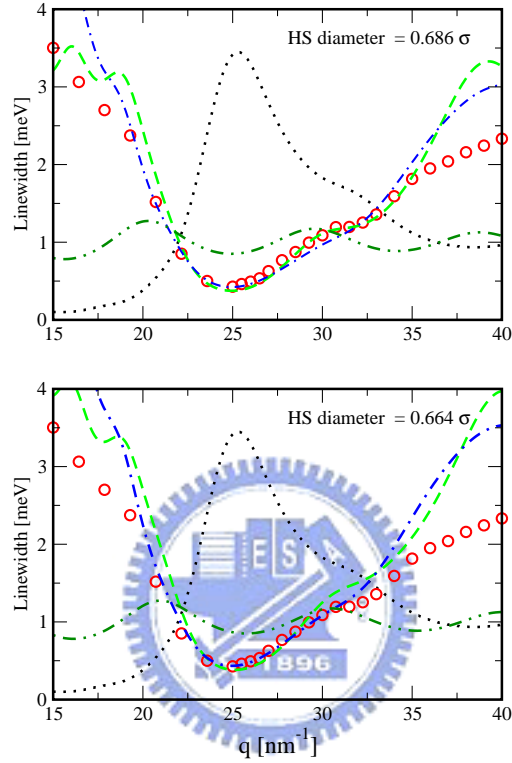


Figure II.11: The linewidth HWHM of $S(q, \omega)$ as a function of q for the simulated liquid of Ga at $T = 323K$. The circles are the results of the liquid simulated with $\phi(r)$ at $T = 323K$. The dotted line is the simulated $S(q)$, the dashed line is the prediction of the revised Enskog theory Eq. II.4, the dotted-dashed line is the prediction of the revised Enskog theory Eq. II.4 without $d(q)$, and the dotted-dotted-dashed line is the $d(q)$ function only. The values of σ_{HS} are 0.686σ in the upper panel and 0.664σ in the lower one.

evaluated by Eq. II.5 is $1.66 \times 10^{-5} \text{cm}^2 \text{s}^{-1}$, which is close to the self-diffusion coefficient $D_s = 1.77 \times 10^{-5} \text{cm}^2 \text{s}^{-1}$ obtained from the velocity autocorrelation function. On the other hand, as σ_{hs} is chosen to be 0.664σ obtained by the E-MCRS theory [33], which accurately predicts the Helmholtz free energy and entropy of the liquid, D_E evaluated by Eq. II.5 is $1.86 \times 10^{-5} \text{cm}^2 \text{s}^{-1}$. The results are not as good as those fitted by 0.686σ : the de Gennes narrowing in the range between $q = 17.5 \text{nm}^{-1}$ and $q = 30.0 \text{nm}^{-1}$ are still described well by revised Enskog theory, but the shoulder is gradually disappeared. Also, shown in Fig. II.11, by comparing the predictions with and without dynamic factor $d(q)$ in Eq. II.4, we find that the $d(q)$, associated with the cage diffusion, cause a quite good fitting between the prediction function and simulated $Z(q)$ for the wavevectors around the shoulder. This information indicates that the mechanism for the occurrence of the shoulder in $Z(q)$ should be related to the cage diffusion. For the single-particle dynamics, the cage diffusion in a liquid usually depicts that a particle is confined in a cage which is composed of its neighbours; therefore, this particle collides with its neighbours in a short timescale but diffuses out of the cage in a longer timescale. Alternatively, from the viewpoint of collective dynamics, the cage diffusion can be considered as the relaxation of the cage structure, with the relaxation time related to the stability of the cage.

Shown in Fig. II.12, to investigate the role of the Friedel oscillations on anomaly in $Z(q)$, we calculate the linewidths $Z_i(q)$ with the pair potentials $\phi_i(r)$ for $i = 0, 1, 2, 3$. Both $Z_0(q)$ and $Z_1(q)$ have a minimum nearby q_M , but they are monotonically ascendent beyond q_M up to 40nm^{-1} , which is close to the first minimum of $S(q)$. This behavior is

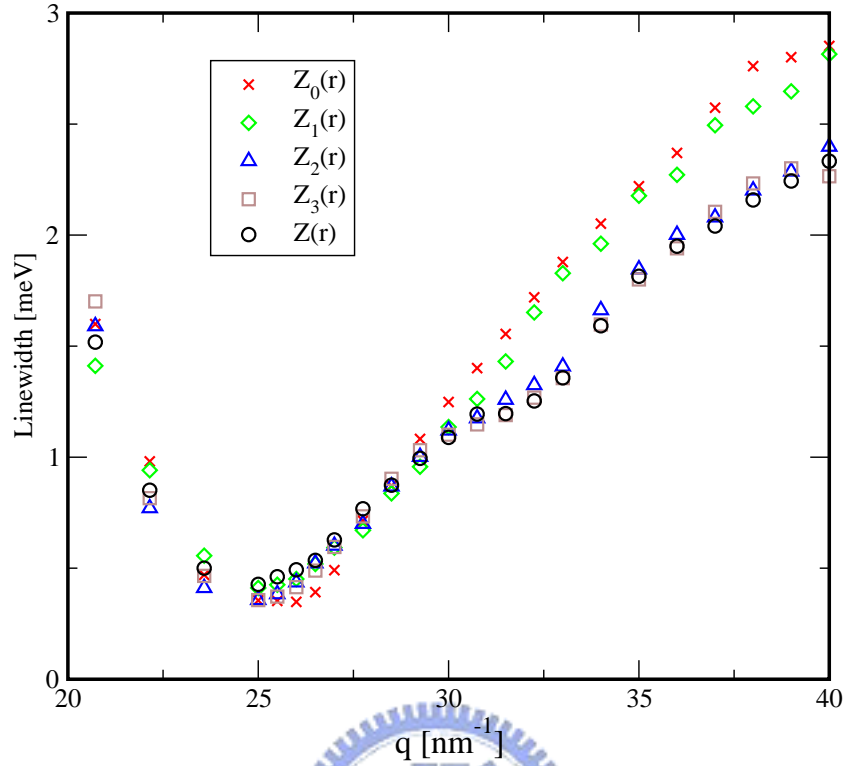


Figure II.12: The spectral linewidth $Z(q)$ for the full-range $\phi(r)$ and $Z_i(q)$ for $\phi_i(r)$ with a finite range. All symbols are the simulated results.

similar as those of the LJ liquids and liquid alkali metals.

As the range of interatomic potential is extended up to the second maximum of the Friedel oscillations, a shoulder clearly appears on the high- q side of the de Gennes narrowing; furthermore, this shoulder is almost developed as well as the one in $Z(q)$ as the range of pair potential is extended up to the third maximum of the Friedel oscillations. In our model, the interaction range of pair potential to produce an anomaly in $Z(q)$ should be farther than the second attractive well; however, this range is shorter than that causing the shoulder in $S(q)$. Fig. II.13 shows that the comparison between the simulated $Z_i(q)$

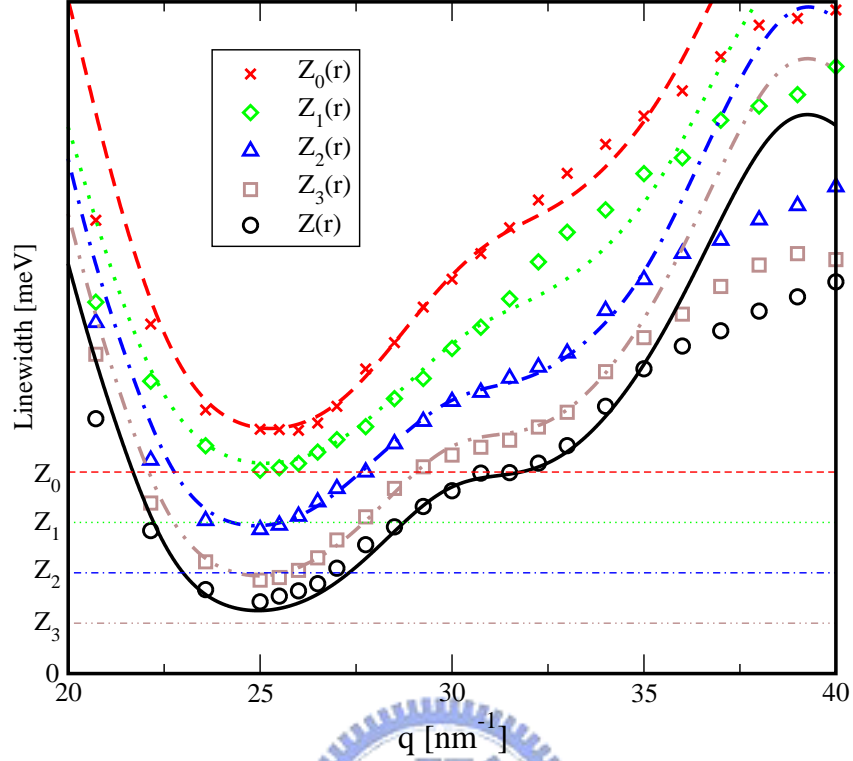


Figure II.13: Comparison between the simulated results (the symbols) and the predictions of the revised Enskog theory with the HS diameter σ_{hs} chosen to be the first-peak position of $g(r)$, D_E evaluated by Eq. II.5 with the chosen σ_{hs} and $S_{hs}(q)$ replaced by $S(q)$ or $S_i(q)$. Each linewidth function for a pair potential is shifted upward 0.3 meV from the lower one.

and the predictions of the revised Enskog theory with the same values of σ_{hs} and D_E , and the $S_{hs}(q)$ in Eq. II.4 replaced by the corresponding $S(q)$ presented in Fig. II.4. Arising from the dynamic factor $d(q)$, a shoulder is indeed produced in the linewidth function $Z_E(q)$, no matter what the range of the pair potential is. The results are consistent with that of Fig. II.13. The shoulder in $Z_2(q)$, $Z_3(q)$ and $Z(q)$ is in good agreement between the prediction of the theory and the simulation result for q from 22.5 nm^{-1} to 35.0 nm^{-1} , but the prediction of the theory for q between 30 nm^{-1} and 35 nm^{-1} is deviated from the

$Z_0(q)$ and $Z_1(q)$, having no shoulder. This is clearly present that the dynamic factor $d(q)$, the characteristic of cage factor, is the essential factor to make the revised Enskog theory a successful prediction for the shoulder in $Z(q)$ [47, 58]. Thus, the shoulder in $Z(q)$ is certainly caused by cage diffusion.

II.5 Conclusions

In this chapter, we use MD simulation with interatomic pair potential ($T = 323K$) obtained from the first-principles GEINMP theory. In the hydrodynamic region, the single Lorentzian-like central peak and the Brillouin peaks of $S(q, \omega)$, the sound velocity of the simulated system, and the damping factor are in good agreement with the experimental results of liquid Ga. On the other hand, we also have successfully produced a shoulder on the high- q side of the first peak in $S(q)$ and an anomaly in the linewidth $Z(q)$ in kinetic region. The shoulder and the anomaly are confirmed to occur at the same location, and they are also consistent with the data of experiment. Our model consists of a ledge-shape repulsive core and the long-range Friedel oscillations induced by the conduction electrons. The shoulder and the anomaly, which have been studied, are the interplay between the effective diameter of the repulsive core and the wavelength of the Friedel oscillations [44]. The results of our simulations indicate that the liquid structures are mainly determined by the ledge-shape repulsive core and the Friedel oscillations, and the shoulder at the high- q side of the first peak in the static structure factor is associated with the appearance of

the solid-like clusters [57]. Moreover, the effective interaction range of the interatomic pair potential that contributes significantly to the shoulder structure should include the first three attractive wells in the Friedel oscillations.

It is well confirmed that sound velocity, with a value of $2850 \pm 20 \text{ms}^{-1}$, of our model for liquid Ga are scarcely dependent on the interaction range. Evidence for collective modes has been found in a q region extending beyond the hydrodynamic regime up to one-half of the main peak structure factor which is about $q = 24.5 \text{nm}^{-1}$.

The anomaly in the linewidth $Z(q)$ of dynamic structure factor can be well described by the revised Enskog theory, with the HS diameter chosen to be the first-peak distance of the radial distribution function. The effective distance of interatomic pair potential to produce the anomaly should include the first two attractive wells in the Friedel oscillations that is different from the effective range to generate the shoulder in the $S(q)$. The characteristic of $d(q)$ implies that the anomaly in $Z(q)$ is caused by cage diffusion [70, 71]. We conclude that the shoulder and the anomaly occur at the same wavevector. In a liquid metal, as the density fluctuations of the positively charged ions have the same wavelength as that of the Friedel oscillations induced by the conduction electrons, the density waves of electrons and ions are coherent. Thus, the overall attractions between the two systems are expected to integrate constructively and enhance the stability of the cage structure of each ion. At temperatures just above the melting point, an enhanced cage structure causes the collective motions a relatively slower relaxation; thus, an anomaly is produced in the $Z(q)$ at the wavenumber of the Friedel oscillations. At high temperature, the

anomaly is expected to disappear because the enhancement is weak and the cage structure is overwhelmed by the thermal motions; this is consistent with the result of liquid Ga measured by QNES experiment [48]. According to our study, we state that the range of our pair potential to produce the dynamic anomaly is shorter than the range to generate the shoulder in the static structure factor, and the dynamic anomaly is a common feature to those polyvalent liquid metals whose static structure factors exhibit a shoulder on the high- q side of the first peak [52].



Chapter III

Hard sphere perturbation theory for liquid Ga

III.1 Introduction

Thermodynamic perturbation theory has played a very important role in the development of the fundamental understanding for dense simple fluids [39, 72]. The success of thermodynamics perturbation theory in describing the properties of fluids is quite sensitive on the choice of a reference fluid. Therefore, the basic principle of perturbation theory is that a model system can be related a reference system, which is much known and its properties can be easily calculated. For example, the structure of a liquid can be described by the reference fluid with the repulsive core only, whereas the attractions are treated as a perturbation. In general, the hard sphere fluid has been the frequently chosen reference fluid because it has well known equation of state, and the pair distribution function can be analytically obtained from the Percus-Yevick equation [30]. The HS reference fluids are appealing both because they are expected to accurately repre-

sent excluded volume (packing) effects and because accurate analytical expressions are available for their thermodynamic and structure properties. However, the HS reference fluids become gradually inaccurate as the describing fluids have very soft repulsive core potential. Some refinements of the theory progress recently, with an aim of applications to soft condensed system.

The Weeks-Chandler-Andersen (WCA) theory [73, 74, 75, 76] can be viewed as a perturbation theory with a soft repulsive reference fluid, whose properties are approximated by a HS fluid. The HS diameter of the WCA theory is determined by the equation of equal compressibility between the reference fluid and the HS fluid. Although the WCA theory has an accurate prediction for fluids, the WCA theory is inaccurate for fluids with very soft repulsive core. According to this serious problem, Lado [77] gives some numerical improvement of the WCA theory with a different choice for the HS diameter. The Mansoori-Canfield [78] and Rasaiah-Stell [79] (MCRS) theory, which is based on a HS reference system and the first-order perturbation, is developed by using the Gibbs-Bogoliubov inequality and treating the HS diameter as a variational parameter to obtain an upper bound of the Helmholtz free energy. This variational HS perturbation theory, has been applied to calculate the structures and thermodynamics of liquid metals, whose effective pair potentials have very soft repulsive cores [80, 81, 82, 44]. However, the MCRS prediction tends to slightly overshoot the simulated Helmholtz free energies, and Mon [27, 83, 84, 31] points out that the inaccurate prediction is a simple consequence of the exclusion of the phase space due to the overlaps of hard spheres in the hard sphere refer-

ence ensemble; therefore, a correction term should be added into the MCRS variational function to improve the accuracy of the variational approach.

The extended MCRS (E-MCRS) theory, developed by Ben-Amotz and Stell [33], include Mon's correction term, and it is found to outperform previous first-order perturbation theories by providing exceptionally accurate predictions of the thermodynamic properties of very soft repulsive fluids. Especially, the E-MCRS theory provides an economically analytical method to predict the thermodynamics properties of the soft repulsive fluids without heavy computations. A key advantage of the perturbative approximation is that the structure of fluids is explicitly retained and thus the excess entropies and packing fractions may be accurately predicted. It is interesting to examine the accuracy of the E-MCRS theory, and other the HS perturbation theories for liquid Ga. We compare the HS perturbation theories by investigating their predictions for the thermodynamic properties of liquid Ga, which are described in Sec. II.2. The density variations of the effective HS diameters of liquid Ga estimated by these theories are investigated and shown; they are the key points in this chapter.

III.2 Theory

III.2.1 The background of E-MCRS theory

A common starting point of various thermodynamic perturbation theories is an expansion of the excess Helmholtz free energy, $A^{ex} = A - A^{IG}$, where A is the total free

energy, and A^{IG} is the free energy of an ideal gas. The excess Helmholtz free energy would be expressed as

$$\frac{A^{ex}}{Nk_B T} = \frac{A_{HS}^{ex}}{Nk_B T} + \frac{\Delta A}{Nk_B T}, \quad (\text{III.1})$$

and $\tilde{A} = A^{ex}/Nk_B T$ of a fluid with N particles also can be expressed as

$$\tilde{A} = \tilde{A}_{HS} + \Delta\tilde{A}, \quad (\text{III.2})$$

with $\tilde{A}_{HS} = A_{HS}^{ex}/Nk_B T$, the free energy of a reference HS fluid, represented by the following Carnahan-Starling [29] expression

$$\tilde{A}_{HS} = \frac{\eta(4 - 3\eta)}{(1 - \eta)^2}, \quad (\text{III.3})$$

where $\eta = \pi\rho\sigma_{HS}^3/6$ is the packing fraction and σ_{HS} is the diameter of particles in the hard-sphere fluid. Finally, $\Delta\tilde{A}$ is the difference of free energy between the fluid of interest and the reference fluid. In the MCRS theory [78, 79], $\Delta\tilde{A}$, derived from the first order perturbation theory, can be approximated

$$\Delta\tilde{A} \approx 2\pi\rho\beta \int_{\sigma_{HS}}^{\infty} g_{HS}(r)\phi(r)r^2 dr, \quad (\text{III.4})$$

where ρ is the system reduced density and $\beta = 1/k_B T$. k_B is the Boltzmann constant and T is temperature. The Ga interatomic pair potential $\phi(r)$, generated from the first-principles generalized energy independent nonlocal modal-pseudopotential (GEINMP) theory [57], is introduced in Sec. II.2.1. The radial distribution function $g_{HS}(r)$ of the hard-sphere (reference) fluid can be analytically obtained by the Verlet algorithm [30].

The MCRS perturbation theory is convenient to apply and provides a rigorous upper bound to the excess Helmholtz free energy. By employing the hard sphere fluid and Gibbs-Bogoliubov inequality, the Eq. III.2 can be represented as

$$\tilde{A} \leq \tilde{A}_{HS} + \Delta\tilde{A}, \quad (\text{III.5})$$

By treating σ_{HS} as a variational parameter, a measured value of \tilde{A} is obtained by minimizing a sum of \tilde{A}_{HS} and $\Delta\tilde{A}$ given in Eqs. III.3 and III.4, respectively.

Mon [27, 83, 84, 31] indicates that a significant part of the residual error in the MCRS theory: arises from the exclusion of a portion of phase space due to the overlap of the hard-sphere. As a hard-sphere reference is used, the perturbation calculation for a fluid model of particles interaction with soft sphere potential $\phi(r)$ contains an intrinsic error. The intrinsic error can be presented as

$$\langle \beta A/N \rangle_{HS} - \beta A/N = \frac{-1}{N} \ln \left[\frac{\int_{\Omega_{HS}} e^{-\beta\phi}}{\int_{\Omega} e^{-\beta\phi}} \right], \quad (\text{III.6})$$

where Ω is the total configurational phase space, and $\langle A/N \rangle_{HS}$ is the free energy as evaluated by sampling over only that part of the phase Ω_{HS} allowed by the hard-sphere reference ensemble, and A/N is the real Helmholtz free energy per particle. Hence, according to Mon's correction term, Eq. III.4 can be rewritten as

$$\Delta\tilde{A} = 2\pi\rho\beta \int_{\sigma_{HS}}^{\infty} g_{HS}(r)\phi(r)r^2 dr - \frac{1}{N} \ln \left[\frac{\int_{\Omega_{HS}} e^{-\beta\phi}}{\int_{\Omega} e^{-\beta\phi}} \right]. \quad (\text{III.7})$$

Recently, Amotz and Stell [33] introduce that the integral ratio of Mon's correction term may be expressed in terms of the following one-dimensional integral over the radial

distribution function of the soft-repulsive part of our model fluid:

$$\frac{-1}{N} \ln \left[\frac{\int_{\Omega_{HS}} e^{-\beta\phi}}{\int_{\Omega} e^{-\beta\phi}} \right] = -2\pi\rho \int_0^{\sigma_{HS}} g(r)r^2 dr. \quad (\text{III.8})$$

$g(r)$ is the radial distribution function of the fluid with the pair potential $\phi(r)$. Therefore,

Eq. III.7 can be replaced by

$$\Delta\tilde{A} = 2\pi\rho\beta \int_{\sigma_{HS}}^{\infty} g_{HS}(r)\phi(r)r^2 dr - 2\pi\rho \int_0^{\sigma_{HS}} g(r)r^2 dr. \quad (\text{III.9})$$

In WCA theory, $g(r)$ can be replaced by

$$g(r) = y_{HS}(r)\exp(-\beta\phi(r)), \quad (\text{III.10})$$

where $y_{HS}(r)$ is the cavity distribution function and can reasonably be represented by the following three term expansion [85]

$$y_{HS}(r) = \exp \left[A + B\left(\frac{r}{\sigma_{HS}}\right) + C\left(\frac{r}{\sigma_{HS}}\right)^3 \right]. \quad (\text{III.11})$$

The values of the three coefficients depend only on the packing fraction, η , of the hard-sphere fluid.

$$A = \frac{3 - \eta}{(1 - \eta)^3} - 3, \quad (\text{III.12})$$

$$B = \frac{-3\eta(2 - \eta)}{(1 - \eta)^3}, \quad (\text{III.13})$$

$$C = \ln \left[\frac{2 - \eta}{2(1 - \eta)^3} \right] - \frac{\eta(2 - 6\eta + 3\eta^2)}{(1 - \eta)^3}. \quad (\text{III.14})$$

In the WCA theory [74], the effective HS diameter σ_{HS} of the model fluid is determined by the solution of the equal compressibility integral equation between the reference fluid

with the repulsive core $\phi_0(r)$ only and a hard-sphere fluid with diameter σ_{HS} at the same temperature and density. The equal compressibility integral equation is given as

$$\int_0^{r_0} y_{HS}(r) \exp(-\beta\phi_0(r)) r^2 dr = \int_{\sigma_{HS}}^{r_0} y_{HS}(r) r^2 dr, \quad (\text{III.15})$$

where r_0 is the position of main attractive well of our model, and the detail derivation is shown as Sec. V.1. In the Lado-WCA method [77], the effective HS diameter is given by the solution of a similar equation, but $y_{HS}(r)$ is replaced by $\partial y_{HS}(r)/\partial\sigma_{HS}$ in both integrands in Eq. III.15. With Eq. III.11[33, 85], the hard-sphere diameter σ_{HS} in these equations can be efficiently solved, and the detail derivation is shown as Sec. V.2.

According to these approximation, a new variational formula of $\Delta\tilde{A}$, referred as the extended-MCRS (E-MCRS) theory, is given as

$$\Delta\tilde{A} = 2\pi\rho\beta \int_{\sigma_{HS}}^{\infty} g_{HS}(r)\phi(r)r^2 dr - 2\pi\rho \int_0^{\sigma_{HS}} y_{HS}(r) \exp(-\beta\phi(r)) r^2 dr. \quad (\text{III.16})$$

The HS diameter for describing $y_{HS}(r)$ in the second integral is determined by the Lado-WCA method and may have a different value from the variational parameter σ_{HS} , which implicitly determines $g_{HS}(r)$ in the integrand of the first integral and appears explicitly in the lower and upper limits of the first and second integrals, respectively. The E-MCRS theory has been shown to give better predictions in thermodynamic properties of the inverse-power fluids than the MCRS and other HS perturbation theories [33].

III.2.2 Thermodynamic Properties

In thermodynamics, the excess Helmholtz free energy \tilde{A} of a fluid at density ρ is related

to the pressure $P(\rho')$ of the fluid at lower density ρ' via the following integration

$$\tilde{A} = \int_0^\rho \left(\frac{\beta P(\rho')}{\rho'} - 1 \right) \frac{d\rho'}{\rho'}. \quad (\text{III.17})$$

$P(\rho')$ can be obtained via the pressure equation:

$$\frac{\beta P(\rho')}{\rho'} = 1 - \frac{4\pi}{6} \beta \rho' \int_0^\infty r \phi'(r) g(r) dr. \quad (\text{III.18})$$

where $g(r)$, the radial distribution function of the fluid at density ρ' is generated by computer simulation, and $\phi'(r)$ is the first derivative of the pair potential. Alternatively, the compressibility factor $Z(\rho) \equiv \beta P/\rho$ also can be written as the Virial series of the density:

$$Z(\rho) = 1 + \sum_{i=2}^{\infty} B_i \rho^{i-1}. \quad (\text{III.19})$$

Here, B_i is the i^{th} Virial coefficient, which is associated with $\phi(r)$ via some diagrams [39]. In the second Virial approximation, $Z(\rho)$ is approximated to be $1 + B_2\rho$ and the calculation of B_2 is straightforward. The excess internal energy is given as

$$\tilde{U} = 2\pi\rho\beta \int_0^\infty r^2 \phi(r) g(r) dr. \quad (\text{III.20})$$

The excess entropy \tilde{S} , which can be evaluated by the difference between the excess internal energy \tilde{U} and the excess Helmholtz free energy \tilde{A} , is presented as

$$T\tilde{S} \equiv \frac{S^{ex}}{Nk_B} = \tilde{U} - \tilde{A}. \quad (\text{III.21})$$

On the other hand, S^{ex} is also defined as the

$$S^{ex} = -(\partial A^{ex}/\partial T)_{N,V}. \quad (\text{III.22})$$

In the MCRS theory, the excess entropy \tilde{S}_{MCRS} is shown as

$$\tilde{S}_{MCRS} = -\frac{\eta(4-3\eta)}{(1-\eta)^2}, \quad (\text{III.23})$$

is simply equal to $-\tilde{A}_{HS}$, which is the excess entropy of a HS fluid with an effective HS diameter of the MCRS value [82]. In the E-MCRS theory, the Mon's correction term gives rise to an extra contribution to \tilde{S}_{MCRS} . After replacing $g(r)$ by $\exp(-\beta w(r))$ into Eq. III.8, \tilde{S} in the E-MCRS theory can be expressed as

$$\tilde{S}_{EMCRS} = -\tilde{A}_{HS} + 2\pi\rho \int_0^{\sigma_{HS}} g(r) [1 + \beta w(r)] r^2 dr, \quad (\text{III.24})$$

where $w(r)$, equal to $-k_B T \ln g(r)$, is the potential that gives the mean force acting on a particle in the fluid. In concept, the mean force between two neighboring particles in a dense fluid includes the direct force due to the interatomic pair potential and an effective force indirectly intermediated through other particles. In general, the indirect force depends on the fluid density, so the potential of mean force at high fluid density can be quite different from the interatomic pair potential. In the Eq. III.24, \tilde{A}_{HS} have the same HS diameter σ_{HS} as that of the upper limit of the integral, and the HS diameter σ_{HS} is obtained by the minimization of variational \tilde{A} in the E-MCRS theory.

III.3 Model and Method

III.3.1 Model

Shown in Fig. III.1, the Ga interatomic pair potential at $T = 323K$, $\phi(r)$, has a

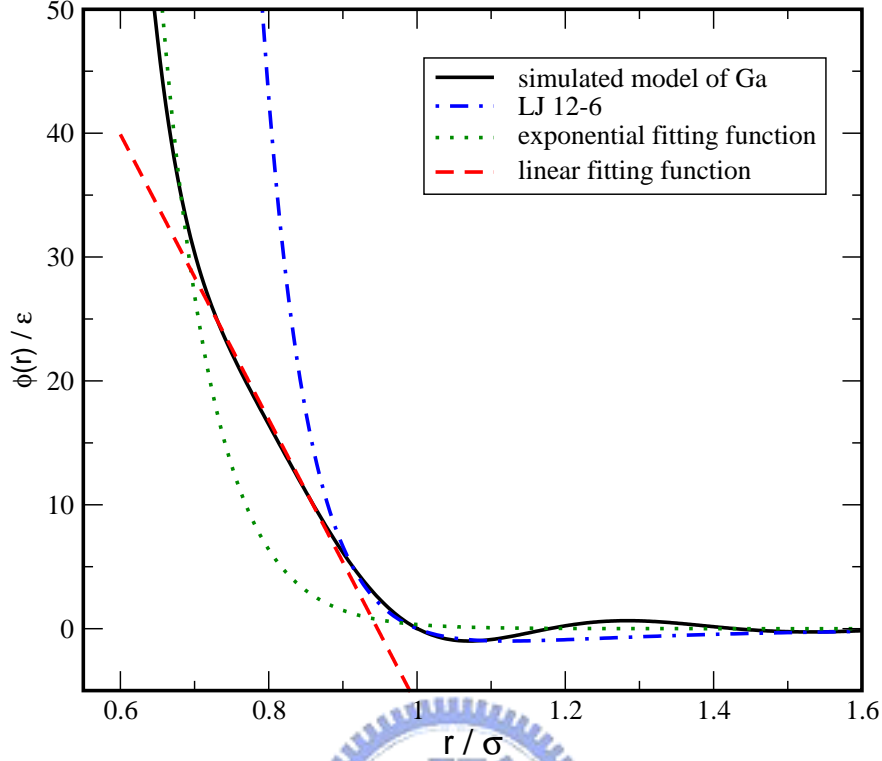


Figure III.1: Interatomic pair potential, $\phi(r)$, (solid line). The dot-dashed line is the LJ potential with the same ε and σ . The dashed line is a linear function $a_1(r/\sigma) + a_2$ with $a_1 = -115$ and $a_2 = 109$; the dotted line is the function $c_1 \exp(-c_2 r/\sigma)(r/\sigma)^{c_3}$, where $c_1 = 4.42 \times 10^6$, $c_2 = 16.4$ and $c_3 = 1.5$

ledge-shape repulsive core and an oscillatory part, whose long-range behavior generally follows the Friedel oscillations [58]. Two parameters of $\phi(r)$ are ε , the depth of the main attractive well, and σ , the shortest distance at $\phi(r) = 0$; the value of ε corresponds to $47K$ and $\sigma = 4.04\text{\AA}$. The repulsive core of $\phi(r)$, denoted as $\phi_0(r)$, is the pure repulsive potential for r smaller than r_0 , which is the position of the main attractive well, and r_0 is about 1.07σ . The pure repulsive potential, $\phi_0(r)$, can be roughly divided into three sections. As r less than 0.7σ , $\phi_0(r)$ increases almost exponentially with decreasing r so

that the repulsive core in this region is extremely stiff. In the intermediate region between 0.9σ and 0.7σ , the value of $\phi_0(r)$ increases roughly from 6ε to 30ε and the shape of $\phi_0(r)$, becoming softer, has a ramp-like behavior with a reflection point around 0.8σ [86]. As r is larger than 0.9σ , $\phi_0(r)$ behaves like the repulsive core of the LJ potential with the same σ and ε , and the interaction potential is less than 6ε [60].

III.3.2 Method

We have carried out a series of molecular dynamics simulations at constant NVT ensemble. In each simulation, we fix the temperature to be 6.85ε which corresponds to $T = 323K$, and the box size is equal to 10.2σ . All quantities given in this chapter are in units of σ , ε and the mass of Ga atom. The number of simulated particles starts at $N = 3500$. Then, in each simulation for a new thermodynamic state, N is reduced by 100, with the lowest N being 100; therefore, we have a series of MD generated configurations at each density. At $N = 3500$, the reduced system density ρ is equal to 3.305, which is close to that of liquid Ga at $T = 323K$ and pressure of about 1 bar. At $\rho = 3.305$, the static and dynamic structure factor of this simulated model agree well with the experimental results at temperature close to the melting point ($T_m = 303K$), and dynamic anomaly of liquid Ga is reproduced [58]. In the following, the thermodynamic properties of the model fluid will be investigated with simulation and various hard-sphere perturbation theories.

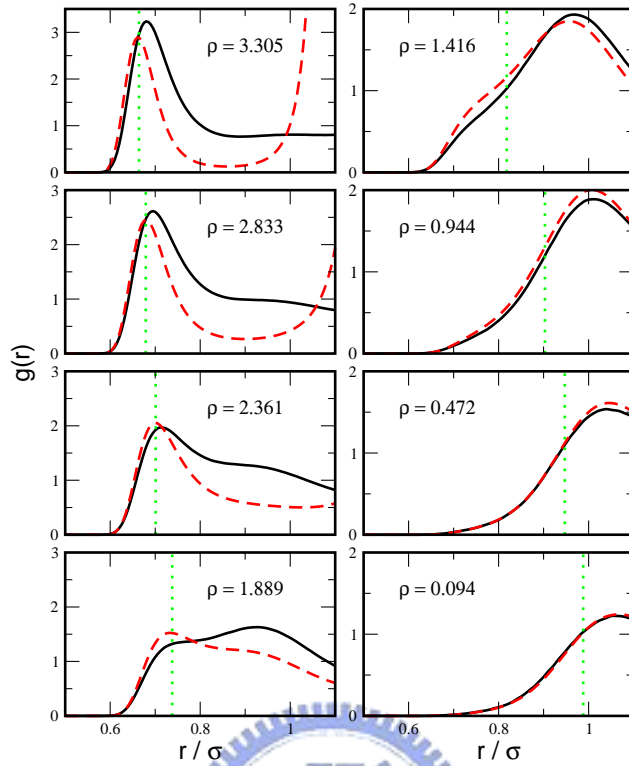


Figure III.2: Radial distribution function of the model fluid at several reduced densities. In each panel, the solid is the simulation result and the dashed line is the approximation given by Eq. III.10 with the Lado-WCA value of σ_{HS} . The dotted line indicates the σ_{HS} value obtained by the E-MCRS theory.

III.4 Results

The radial distribution functions of these simulated systems at various reduced system density are shown in Fig. III.2. At $\rho = 3.305$, the main peak of $g(r)$ is located at 0.686σ , well inside the repulsive core of $\phi(r)$. By decreasing ρ , the main peak of $g(r)$ gets lower and shifts outwardly, and a shoulder near σ appears and grows. Moreover, around $\rho = 2.0$, the roles of the main peak and the shoulder exchange, because the main peak occurs near

σ and the shoulder resides in the inner side of the repulsive core. As ρ keeps on decreasing, the in-inside shoulder finally disappears at $\rho = 1.35$. The new main peak near σ keeps the same shape and moves toward the position of the first attractive well with decreasing ρ . Similar results of the variation of $g(r)$ with density are also observed for the one-scale and two-scale ramp potentials [87], introduced by Jagla [88]. On the other hand, the approximation in Eq. III.10 for our model fluid are examined by evaluating $y_{HS}(r)$ in the approximate Eq. III.11 with the Lado-WCA HS diameter for some reduced densities, and the results are also shown in Fig. III.2. For each density, Eq. III.10 is only good for $g(r)$ inside the value of σ_{HS} , which is obtained by the E-MCRS theory; however, in following, the calculations need the contributions of $g_{HS}(r)$ inside the σ_{HS} .

$w(r)$, giving the mean force acting on a particle in the fluid, is the other way to manifest the density effect on the variation of $g(r)$ in our model. The definition of $w(r)$ have been given in Section. III.2.2, and the variation of $w(r)$ with reduced density ρ is shown in Fig. III.3. At $\rho = 3.305$, because of the high compactness in the fluid, $w(r)$ has a deep attractive well, which is at the first-peak position of $g(r)$. Furthermore, the depth of this attractive well gradually reduces and a shoulder near σ appears by decreasing ρ . Around $\rho = 1.889$, the roles of this attractive well and the shoulder in $w(r)$ switch with each other, as the similar case in Fig. III.2. Beginning at $\rho = 1.889$, the new attractive well in $w(r)$ continuously moves out and the new attractive well become deep. Finally, the well is attenuated to ε .

Fig. III.4 shows the variation with density of the HS diameter, which are estimated

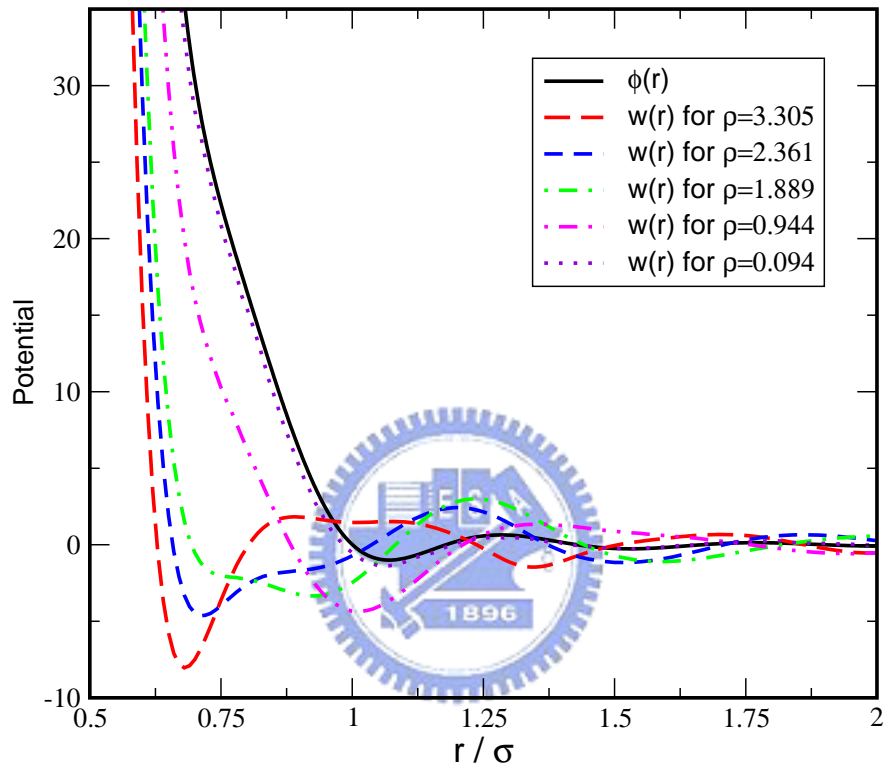


Figure III.3: Potential of mean force $w(r)$ of the model fluid at $\rho = 3.305$ (dashed line), $\rho = 2.361$ (short-dashed line), $\rho = 1.889$ (dot-dashed line), $\rho = 0.944$ (dot-dot-dashed line) and $\rho = 0.094$ (dotted line). The solid line is the interatomic pair potential $\phi(r)$. All potentials are scaled with ε and distance is scaled with σ .

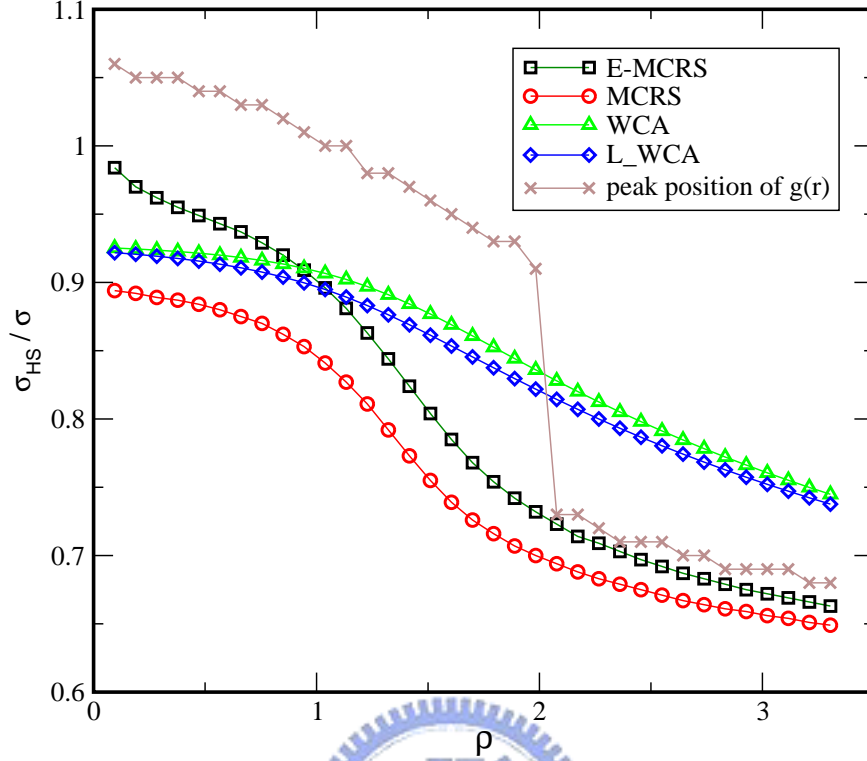


Figure III.4: The variation of effective HS diameter σ_{HS} as a function of density. σ_{HS} is estimated by the WCA (triangles), Lado-WCA (diamonds), MCRS (circles) and E-MCRS (squares) theories. The crosses stand for the main-peak position of $g(r)$.

by the E-MCRS, MCRS, WCA, and L-WCA theories. The values of the HS diameter estimated by the four perturbation theories decrease with increasing density, and our results are consistent with the results that the effective HS diameter of a fluid is decreased with increasing the fluid density [33]. At high densities, both WCA and L-WCA σ_{HS} values are larger than the main-peak position of $g(r)$, which is inside the repulsive core; however, the HS diameters become smaller than the position of main-peak of $g(r)$ below $\rho = 2.0$. Not only the σ_{HS} values of the MCRS theory is limited by the peak position of $g(r)$ but also the E-MCRS value is almost along the track of the peak position as ρ

is larger than 2. According to Fig. III.1, as the density is below $\rho = 2.0$, because the exponential-like behavior of average distance between particles is replaced by ramp-like behavior, the position of the main-peak of $g(r)$ makes a jump to a larger value around $\rho = 2.0$. Therefore, the HS diameters of the MCRS and E-MCRS theory are apparently released from the restriction due to the main-peak position of $g(r)$ and ascend manifestly as ρ varies from 2 to 1. The MCRS value is roughly fixed at 0.9σ as density approaches to zero, but the E-MCRS value continuously increases at very low densities and passes over the values of the WCA and Lado-WCA theories.

According to the pressure equation, the compressibility factor $Z(\rho)$ can be calculated, and the results are shown by symbols in Fig. III.5. In order to perform numerical integration of $Z(\rho)$, we fit $Z(\rho)$ in Fig. III.5 with the series in Eq. III.19 truncated beyond the fourth order of ρ and treat the virial coefficients as fitting parameters. The simulated data of $Z(\rho)$ can be separated into two parts. One is larger than $\rho = 1$ and the other is smaller than $\rho = 1$, and we give the values of the fitting parameters in the caption of Fig. III.5. The inset of Fig. III.5 shows the second Virial approximation that check the accuracy of our calculations at low densities.

In the MCRS and E-MCRS theories, the variational curves of excess Helmholtz free energy \tilde{A} for some reduced densities are shown in Fig. III.6, and each curve has a minimum, which corresponds to a HS diameter. In these two theories, the approximate $g_{HS}(r)$, obtained by Verlet algorithm [30], is used, and $y_{HS}(r)$ is approximated by Eq. III.11 with the Lado-WCA σ_{HS} value. In E-MCRS theory, Mon's correction term causes the mini-

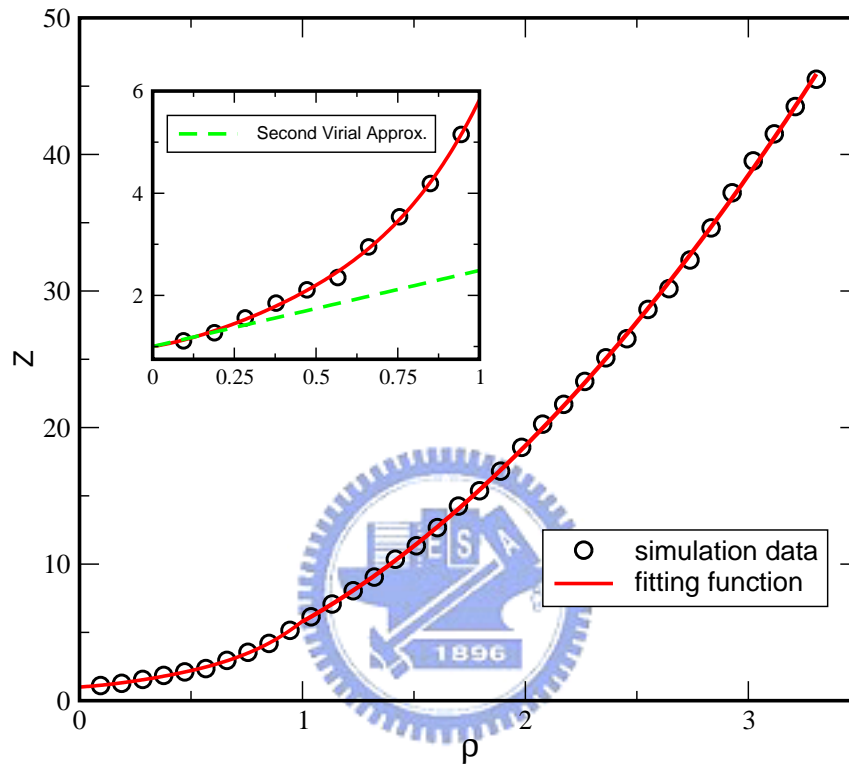


Figure III.5: Compressibility factor, $Z = \beta P/\rho$, as a function of density. The circles are calculated by the pressure equation with the simulated $g(r)$. The solid line is the Virial function III.19 with the Virial parameters: $B_2 = 0.995$, $B_3 = 4.129$, $B_4 = -4.969$, and $B_5 = 4.67$ for $\rho > 1$, and $B_2 = -0.323$, $B_3 = 5.228$, $B_4 = -0.523$, and $B_5 = 0.055$ for $\rho < 1$. The inset shows Z at low densities and the second virial approximation (dashed line).

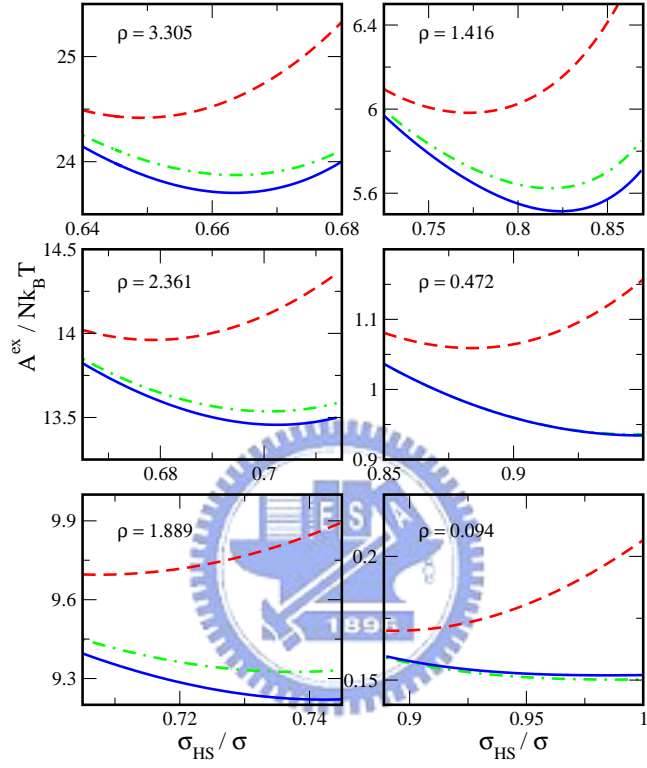


Figure III.6: Variation of $A^{ex}/Nk_B T$ on σ_{HS} at the indicated reduced density. In each panel, the solid and dashed lines are the curves for the E-MCRS and MCRS $A^{ex}/Nk_B T$, respectively. The dot-dashed line is the variational $A^{ex}/Nk_B T$ with Mon's correction term given in Eq .III.8. At $\rho = 0.472$ and $\rho = 0.094$, the solid and dot-dashed lines are almost the same.

mum of the variational curve shifting to a larger effective HS diameter and a lower value of \tilde{A} than those obtained by the MCRS theory. These results are expected to be true for all kinds of fluid [33]. The accuracy of the approximation in Eq. III.10 is examined again by calculating excess Helmholtz free energy. In Fig. III.6, although the corresponding variational curve of Eq. III.9 generally shifts upward relative to the one of Eq. III.16, the HS diameter σ_{HS} , which is estimated by Eq. III.9 is the same as that, which is estimated by Eq. III.16, and the overall thermodynamics properties of our calculation are not effected. By using the fitting function Eq. III.19, we have done the integration in Eq. III.17 and the results are indicated by the symbols in Fig. III.7. Shown in Fig. III.7, the excess Helmholtz free energies estimated by the various HS perturbation theories, including the WCA, L-WCA, MCRS and E-MCRS theories, and the comparison between these results is presented. Although the MCRS prediction slightly deviates from the simulated excess Helmholtz free energy, Mon's correction cause the E-MCRS prediction to match the simulated data well for entire densities. Apparently, the variational approaches do a better prediction than the WCA [73, 74, 75, 76] and Lado-WCA [77] theories, which are only good for the region of $\rho < 1$.

Fig. III.8 shows the behaviors of simulated and approximate excess entropies \tilde{S} . In thermodynamics, \tilde{S} has a linear behavior at low densities because the excluded volume effect due to the repulsive core of $\phi(r)$. Intriguingly, the density curve of \tilde{S} has a small positive slope in the intermediate range, which is roughly from $\rho = 1.4$ to 1.8. The anomalous behavior of excess entropy is also observed in a two-scale ramp potential [89].

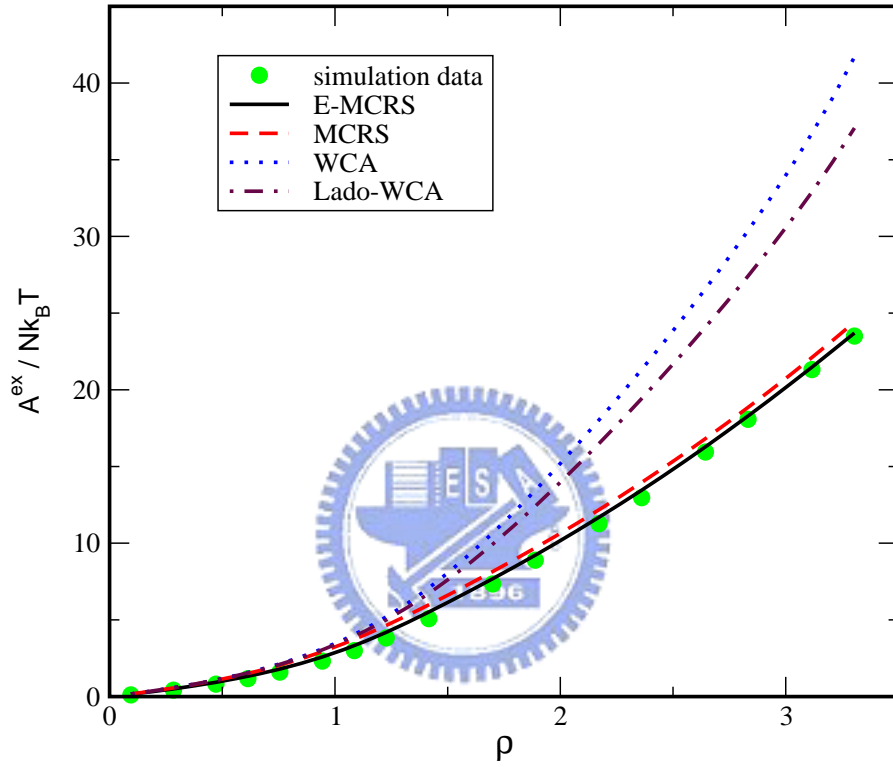


Figure III.7: The excess Helmholtz free energy $\tilde{A} = A^{ex}/Nk_B T$ predicted by the E-MCRS (solid line), MCRS (dash line), WCA (dotted line) and Lado-WCA (dot-dashed line) theories and the result calculated by Eq .III.17 (symbols).

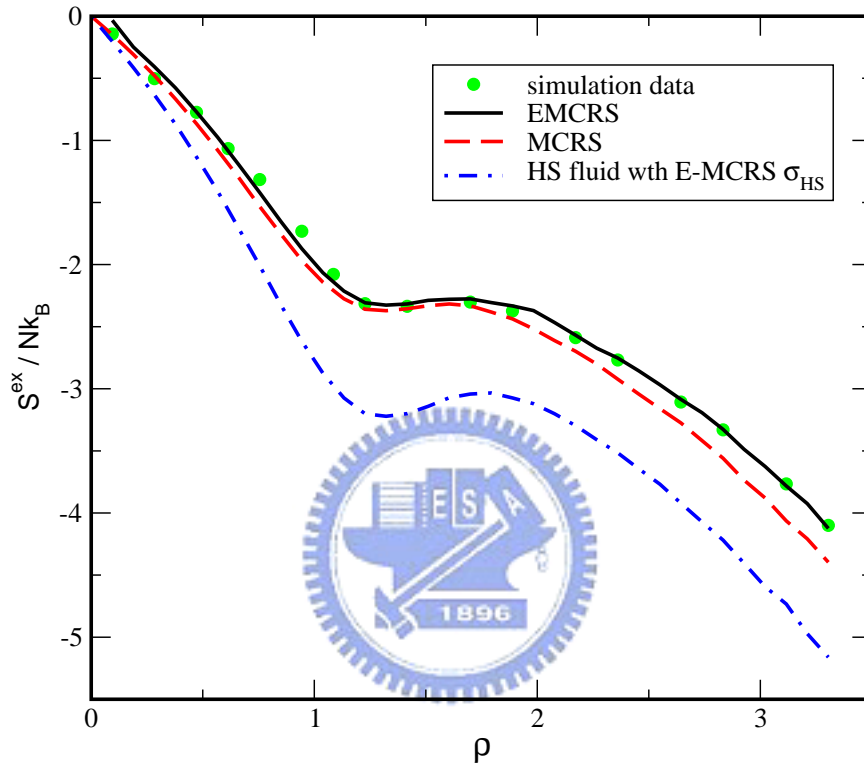


Figure III.8: Density dependence of the excess entropy $\tilde{S} = S^{ex}/Nk_B$. The solid and dashed lines are the predictions of the E-MCRS and MCRS theories, respectively. The dot-dashed line is the HS-fluid contribution in the E-MCRS theory. The symbols are the results of thermodynamic calculation.

Beyond the intermediate region, \tilde{S} decrease with density in a slower decreasing rate, because the density effect is more significant than the diameter reduced effect again. In approximation, the prediction of the MCRS theory agrees well with the result of thermodynamic calculation at low densities, and also has smaller values of excess entropy anomaly in the intermediate range; however, the excess entropy of MCRS's prediction are deviated from simulation data at higher densities. As the E-MCRS diameter is substituted into Eq. III.23, which is the excess entropy of a HS fluid, the absolute value of the excess entropy with a manifested anomaly is larger than that estimated by the MCRS theory. It is amazing that the Mon's correction in Eq. III.24 makes the prediction of the E-MCRS theory have a triumph over the MCRS theory for a perfect agreement with the simulation results in the entire density. It is easy to be understood: The contribution of Mon's correction becomes gradually larger with increasing density; thus, Mon's correction is more important at higher densities and it gives a fundamental improvement of the HS variational prediction for the excess entropy of a fluid.

Fig. III.9 shows the density dependence of the packing fraction η of the HS fluid estimated by various perturbation theories. For either the WCA or the Lado-WCA value of σ_{HS} , the η increases monotonically with increasing density; however, their η values are over 0.7 at reduced system density $\rho = 3.305$, which is close to the density of realistic liquid Ga. The large packing fraction, which is in the solid phase of the HS system, indicate that the overestimation of the effective HS diameter makes the reference HS fluid too much deviate from realistic liquid Ga. On the other hand, due to the values of σ_{HS} in Fig. III.4

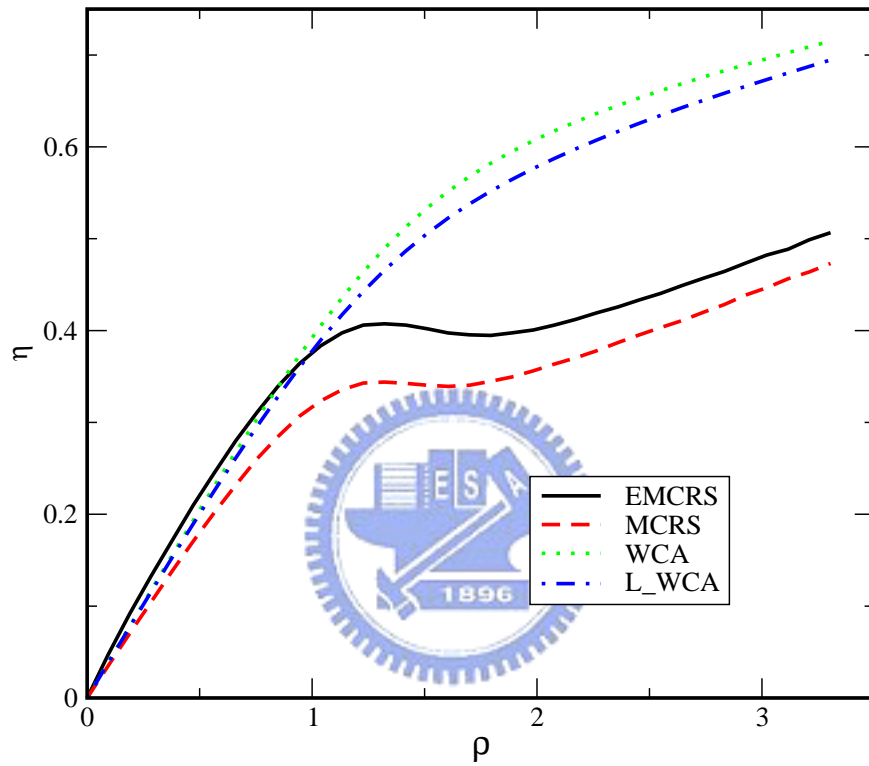


Figure III.9: Density dependence of packing fraction η of the HS fluid with HS diameter of the E-MCRS (solid line), MCRS (dashed line), WCA (dotted line) and L-WCA (dot-dashed line) values shown in Fig .III.4.

estimated by the MCRS and E-MCRS theories, the packing fraction ($\eta = \pi\rho\sigma_{HS}^3/6$) of the MCRS theory is reasonably smaller than that of the E-MCRS theory. In following, we explain that why the anomaly in \tilde{S} predicted by the MCRS and E-MCRS theories occurs in our model. In Fig. III.9, the density curves of MCRS and E-MCRS theories also have apparently a anomaly, which shows a negative slope from $\rho = 1.3$ to 1.7. We maintain that the negative slope corresponds to the substantial shrinkage in the size of the effective HS with increasing density at this region as shown in Fig. III.4; thus, the anomaly appears in the packing fraction and the same physical picture cause the occurrence of anomaly in excess entropy for MCRS and E-MCRS theories. Beyond this anomaly region, the η continuously increases and \tilde{S} continuously decrease, because the contribution of density effect more than that of particle size effect. In the E-MCRS and MCRS theories, the η of the HS reference systems at $\rho = 3.305$ is close to the physically reasonable values: 0.473 and 0.5, which are in the fluid-solid coexistence region of the HS system.

III.5 Conclusions

The interatomic pair potential of liquid Ga model has a ledge-shape repulsive core and a long-range oscillatory part induced by conduction electrons. We have investigated thermodynamic properties of this model fluid to investigate the applicability of some HS perturbation theories which include the WCA, Lado-WCA, MCRS and E-MCRS approximations. These approximate methods have been used for the Lennard-Jose, inversed-

power fluids and liquid Na. The MD simulations of our model fluid at constant NVT ensemble from low to high densities are performed, and the highest density corresponds to realistic liquid Ga at $T = 323K$. There is an interesting above the density variation of the model fluid: The main peak of the radial distribution function is located in the repulsive core region of the interatomic pair potential at high density, the position of the main peak suddenly jumps to a larger distance at some intermediate density and the main peak moves outwardly to the first attractive well of the interatomic pair potential as the density is continuously decreased.

Although the WCA and Lado-WCA methods are accurate for the Lennard-Jones fluids, the predicted HS diameters are too large for our model at high densities. The packing fractions in the WCA and Lado-WCA theories are over the freezing point of the HS reference system so that they are failure for realistic liquid Ga. Based on a variational approach, the MCRS and E-MCRS theories take into account the effect of the anomaly of packing fraction in a region of intermediate density, and the HS reference systems for the model fluid are physically reasonable at entire density. According to the deficiency of the HS perturbation theory, Mon gives a correction which is related to the configuration space of the hard-sphere fluid. Considering this correction, the E-MCRS theory indeed improves the predictions on the thermodynamics properties of the model fluid: the estimated Helmholtz free energy and entropy by E-MCRS method are closer to the simulation results than those by others methods. An anomalous region, associated with the shrinkage of the effective HS diameter by increasing system density, is found in the excess entropy of our

model varied with density. For the predictions of the thermodynamic properties of liquid Ga, our results suggest that the E-MCRS perturbation theory is the most accurate one in all HS perturbation theories.



Chapter IV

Conclusions

In this thesis, the model of simulation is a gallium interatomic pair potential, which consists of a ledge-shape repulsive core and the long-range Friedel oscillations induced by the conduction electrons, is obtained from the first-principles GEINMP theory at the thermodynamic conditions of liquid gallium close to the melting point. The repulsive core of the pair potential varies continuously from an exponential-decay inner core, through a ramp-like intermediate region, to a LJ-like outer core. By MD simulation, we have successfully reproduced the static structure factor and dynamic structure factor which agree well with the results of experiments; further, the structures, dynamic properties, and thermodynamic properties of this pair potential have been investigated for studying the realistic liquid gallium. We summarize the conclusions in the following.

In chapter II, a shoulder appears on the high- q side of the first peak in the static structure factor and an anomaly appears on the linewidth of dynamic structure factor, in good agreements with the experimental data of liquid gallium. According to our results,

the structure anomaly is determined by the ledge-shape repulsive core and first three attractive well. In local structure, a modulation produced by the Friedel oscillation makes the appearance of some solid-like cluster, which are, in concept, more or less like the Peierls-distortion mechanism proposed for liquid-Arsenic before [90, 91]. It is suggested that the shoulder in the static structure factor is associated with the appearance of these solid-like clusters.

Also, the anomaly in the linewidth of the dynamic structure factor is determined by the ledge-shape repulsive core and the first two attractive wells. The dynamic anomaly, which can be well described by the revised Enskog theory with the HS diameter determined by the first-peak distance of the radial distribution function, is interpreted by cage diffusion. The structure and dynamic anomaly are confirmed to occur at the same wavenumber, which suggests that the ion-density fluctuation at this wavevector has the same wavelength with the Friedel oscillations induced by the conduction electrons. Thus, at this wavevector, the density waves of ions and electrons are coherent and the attractions between the two systems would be more rigid so that the cage around each ion becomes harder.

In chapter III, the radial distribution function of the model has an interesting variation with number density: At high density, the main peak of the radial distribution function is located in the inner region of the repulsive core with an exponential decay. At some critical density, the position of the main peak makes a discontinuous jump to the outer core of the LJ-like region. As the density is further decreased, the main peak moves toward the minimum of the first attractive well of the pair potential.

To predict the thermodynamic behaviors of our model, the WCA, Lado-WCA, MCRS and E-MCRS methods are used. For the prediction of HS diameter, the packing fractions, which are estimated by the WCA and the Lado-WCA methods, are over the freezing point of the HS system and this makes the WCA and Lado-WCA theories breakdown for our model at high densities. In MCRS and E-MCRS theories, due to the estimated HS diameter is obviously reduced in a region of intermediate density, the density curve of the packing fraction has a negative slope in this region; further, beyond this density region, the value of packing fraction is physically reasonable at high density. The E-MCRS theory, which includes Mon's correction to improve the MCRS theory, can predict the better results of the excess Helmholtz free energy and the excess entropy than those predictions of the WCA, Lado-WCA and MCRS theories. Furthermore, the anomalous behavior of excess entropy in our model can be described by the E-MCRS and EMCRS theories, and the anomaly is associated with the substantial reduction of the effective HS diameter estimated by the two variational theories.

Chapter V

Appendix

V.1 WCA Theory

Considering a Lennard-Jones potential of the 6-12 type

$$\phi(r) = 4\epsilon \left[(\sigma/r)^{12} - (\sigma/r)^6 \right], \quad (\text{V.1})$$

where σ is the dimensions of length, and ϵ the dimensions of energy. The structure of the Lennard-Jones system is conveniently described in terms of the two-particle correlation function and its Fourier transform. The correlation function is $h(r) = g(r) - 1$, where $g(r)$ is the usual radial distribution function. The dimensionless Fourier transform of the correlation function is

$$h(k) = \rho \int h(r) \exp(-i\mathbf{k} \cdot \mathbf{r}) \, d\mathbf{r}. \quad (\text{V.2})$$

The structure factor, $S(k)$, is simply $h(k) + 1$, and it is measured directly by scattering experiments performed on a fluid.

Weeks, Chandler and Andersen state two hypotheses: (1) At intermediate and large wavevectors ($k\sigma \geq \pi$), the quantitative behavior of $h(k)$ is dominated by the repulsive forces (the attractive forces are primarily manifested in the small wavevectors portion of the spectrum); (2) For high densities ($\rho\sigma^3 \geq 0.65$), the behavior of $h(k)$ even at small wavevectors ($k\sigma \leq \pi$) is at least qualitatively determined by the repulsive forces. For the first statement, $h(k)+1$ represents the linear response of the fluid structure to a disturbance of wavelength $2\pi/k$. While a short wavelength disturbance will probe both the repulsive and attractive forces in a fluid, it is reasonable that the harsh repulsions, rather than the slowly varying longer range attractions, will dominate the response of the fluid to such a disturbance. The second statement is equivalent to asserting that the correlations in a simple liquid are almost entirely due to excluded volume effects when the density is high.

For the first step of WCA theory, the Lennard-Jones potential can be separated into two parts:

$$\phi(r) = \phi_0(r) + \Delta\phi(r), \quad (\text{V.3})$$

where $\phi_0(r)$ is the reference system pair potential, and $\Delta\phi(r)$ is the perturbation potential. For the particular separation in which we are interested, $\phi_0(r)$ includes all the repulsive forces in the Lennard-Jones potential and $\Delta\phi(r)$ all the attractions. With the additional condition that the reference system pair potential obey the thermodynamic requirement $\phi_0(r) \rightarrow 0$ as $r \rightarrow \infty$, this separation is unique:

$$\phi_0(r) = \begin{cases} \phi(r) + \epsilon, & \text{for } r < 2^{1/6}\sigma \\ 0, & \text{for } r \geq 2^{1/6}\sigma \end{cases} \quad (\text{V.4})$$

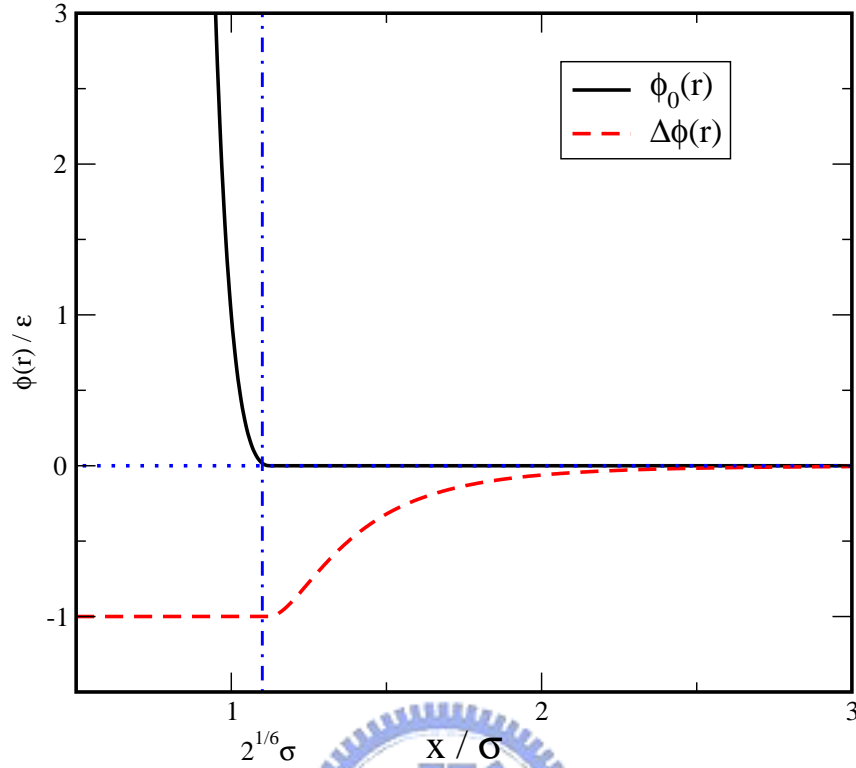


Figure V.1: Separation of the Lennard-Jones potential, $\phi(r)$, into a part containing all the repulsive forces, $\phi_0(r)$, and a part containing all the attractive forces, $\Delta\phi(r)$. dotted-dashed line is the position of $2^{1/6}\sigma$

$$\Delta\phi(r) = \begin{cases} -\epsilon, & \text{for } r < 2^{1/6}\sigma \\ \phi(r), & \text{for } r \geq 2^{1/6}\sigma. \end{cases} \quad (\text{V.5})$$

These functions are shown in Fig. V.1.

The thermodynamic ramifications of postulate of the WCA theory have been discussed.

First, considering the free energy, this is done by introducing a "test" potential

$$\phi(r; \lambda) = \phi_0(r) + \lambda\Delta\phi(r), \quad 0 \leq \lambda \leq 1 \quad (\text{V.6})$$

Then, it can relate the Helmholtz free energy of the Lennard-Jones system to the reference

system and the perturbation:

$$A^{ex}/Nk_B T = A_0^{ex}/Nk_B T + \rho/(2k_B T) \int_0^1 d\lambda \int g(r; \lambda) u(r) d\mathbf{r}. \quad (\text{V.7})$$

Here $g(r; \lambda)$ is the radial distribution function in the "test" system, A^{ex} is the excess free energy, A_0^{ex} is the excess free energy in the reference system. With the choice of reference and perturbation interactions, the integral over λ in Eq. V.7 represents the effect of turning on the attractive forces in the Lennard-Jones fluid: when $\lambda = 0$, $g(r; \lambda)$ is the radial distribution function for the reference system, $g_0(r)$; and $\lambda = 1$, $g(r; \lambda)$ is the Lennard-Jones $g(r)$. According to the WCA hypothesis, when the density is sufficiently high, $g(r)$ is accurately approximated by $g_0(r)$, and we introduce the function $y_0(r)$ which is defined by the equation

$$g_0(r) = y_0(r) \exp[-\beta\phi_0(r)]. \quad (\text{V.8})$$

Physically, $y_0(r)$ gives the correlations that exist in the reference system beyond the range of the reference interaction. Since this interaction is harshly repulsive, it seems probable that $y_0(r)$ can be approximated by the similar function appropriate to a hard-sphere system of diameter σ_{HS} , $y_{HS}(r)$. For this reason, we consider the following approximation:

$$g_0(r) \cong y_{HS}(r) \exp[-\beta\phi_0(r)]. \quad (\text{V.9})$$

Therefore, a reference system potential $\phi_0(r)$, which Boltzmann factor $e_0(r) = \exp[-\beta\phi_0(r)]$, is harshly repulsive but continuous. The Boltzmann factor of reference system is not very different from the Boltzmann factor $e_{HS}(r) = \exp[-\beta\phi_{HS}(r)]$ of a hard sphere potential,

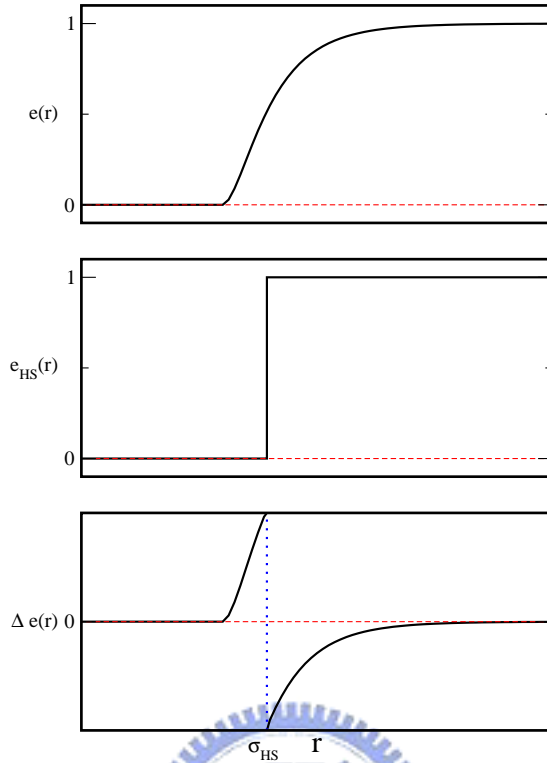


Figure V.2: The "blip function". The quantities $e(r)$ and $e_{HS}(r)$ are the Boltzmann factors, respectively, for soft-core and hard-core potentials.

and ϕ_{HS} is the hard sphere repulsion of diameter σ_{HS} . Thus, for a properly chosen value of σ_{HS} , the function

$$\Delta e(r) = e_0(r) - e_{HS}(r) \quad (\text{V.10})$$

is effectively non-zero over only a small range of r , and it is shown as Fig. V.2

Consider a function $B(r)$, which is a difference between $g_0(r)$ and $g_{HS}(r)$, is defined as

$$g_0(r) = g_{HS}(r) + B(r) \quad \text{or} \quad B(r) = y_{HS}(r) \Delta e(r). \quad (\text{V.11})$$

where $g_{HS}(r)$ is the radial distribution function of hard sphere fluid. By taking Fourier transforms, the hypothesis of WCA theory verify that $h(k) \cong h_0(k)$ is for some range of wavevector,

$$h_0(k) = h_{HS}(k) + \rho \int y_{HS}(r) [\exp(-\beta\phi_0(r)) - \exp(-\beta\phi_{HS})] \exp(-i\mathbf{k} \cdot \mathbf{r}) \mathbf{dr}, \quad (\text{V.12})$$

where $h_0(k)$ is the Fourier transform of the reference system two-particle correlation function, and σ_{HS} is determined by vanishing the integral term. Since $B(r)$ is almost zero except near $r = \sigma_{HS}$. So, the integral term of Eq. V.12 can be represented as

$$\int_0^\infty y_{HS}(r) [\exp(-\beta\phi_0(r)) - \exp(-\beta\phi_{HS})] r^2 dr = 0, \quad (\text{V.13})$$

where

$$\exp[-\beta\phi_0(r)] = \begin{cases} \exp[-\beta\phi_0(r)], & \text{for } r < 2^{1/6}\sigma \\ 1, & \text{for } r > 2^{1/6}\sigma \end{cases} \quad (\text{V.14})$$

$$\exp[-\beta\phi_{HS}(r)] = \begin{cases} 0, & \text{for } r < \sigma_{HS} \\ 1, & \text{for } r > \sigma_{HS}. \end{cases} \quad (\text{V.15})$$

For $0 < \sigma_{HS} < 2^{1/6}\sigma$,

$$\int_0^{\sigma_{HS}} y_{HS}(r) \exp[-\beta\phi_0(r)] r^2 dr = \int_{\sigma_{HS}}^{2^{1/6}\sigma} y_{HS}(r) [\exp(-\beta\phi_0(r)) - 1] r^2 dr, \quad (\text{V.16})$$

finally,

$$\int_0^{2^{1/6}\sigma} y_{HS}(r) \exp[-\beta\phi_0(r)] r^2 dr = \int_{\sigma_{HS}}^{2^{1/6}\sigma} y_{HS}(r) r^2 dr. \quad (\text{V.17})$$

For our potential of liquid Ga, the position of r_0 corresponds to the position of $2^{1/6}\sigma$ of 6-12 Lennard-Jones potential.

V.2 Lado-WCA Theory

The combination of Eq. V.9 and Eq. V.17 produce good results when apply to the hard repulsive part of the Lennard-Jones potential, but is less successful with the softer repulsive potential. A fundamental shortcoming inherent in this combination is the lack of thermodynamic consistency; thus, the pressure P obtained from the free energy A ,

$$\frac{\beta P}{\rho} = \rho \frac{\partial(\beta A/N)}{\partial \rho}, \quad (\text{V.18})$$

is not the same as that found through the usual quadrature,

$$\beta P/\rho = 1 - \rho/6 \int g(r)\phi'(r)rdr, \quad (\text{V.19})$$

the former being more accurate.

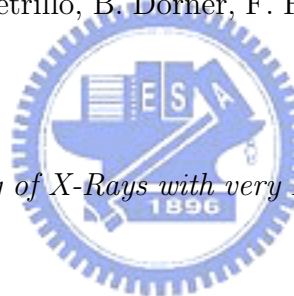
In this note, Load shows that the basic approximation, Eq. V.13, can be obtained by minimizing an approximate expression for the free energy. A production of this approach is a new criterion for choosing the hard sphere diameter, namely

$$\int \{\exp [-\beta\phi(r)] - \exp [-\beta\phi_{HS}(r)]\} \frac{\partial y_{HS}(r)}{\partial \sigma_{HS}} d\mathbf{r} = \mathbf{0}, \quad (\text{V.20})$$

which eliminates the disagreement between Eq. V.18 and Eq. V.19 and leads to improvements in the computed results. Because it implies thermodynamic consistency, Eq. V.20 is the formal implementation of the Verlet-Weis [92] criterion.

Bibliography

- [1] J. R. D. Copley and M. Rowe, *Phys. Rev. A.* **9**, 1656 (1974).
- [2] F. J. Bermejo, M. L. Saboungi, D. L. Price, M. Alvarez, B. Roessl, C. Cabrillo and A. Ivanov, *Phys. Rev. Lett.* **85**, 106 (2000).
- [3] L. E. Bove, F. Sacchetti, C. Petrillo, B. Dorner, F. Formiscano and F. Barocchi, *Phys. Rev. Lett.* **87**, 215504 (2002).
- [4] E. Burkel, *Inelastic Scattering of X-Rays with very High Energy Resolution* (Springer-Verlag, Berlin, 1991).
- [5] P. Chieux, J. Dupuy-Philon, J. F. Jal and J. B. Suck, *J. NonCryst. Solids.* **205-207**, 370 (1966).
- [6] P. Verkerk, P. H. K. De Jong, M. Arai, S. M. Bennington, W. S. Howells and A. D. Taylor, *Physica B* **180,181**, 834 (1992).
- [7] C. Morkel and W. Glaser, *Phys. Rev. A.* **33**, 3383 (1986).



- [8] A. G. Novikov, V. V. Savostin, A. L. Shimkevich and R. M. Yulmetyev, *Physica B* **128**, 312 (1996).
- [9] T. Bodensteiner, C. Morkel, W. Glaser and B. Dorner, *Phys. Rev. A* **45**, 5709 (1992).
- [10] T. Scopigno, U. Balucani, G. Ruocco and F. Sette, *Phys. Rev. E* **63**, 011210 (2000).
- [11] T. Scopigno, A. Filipponi, M. Krisch, G. Monaco, G. Ruocco and F. Sette, *Phys. Rev. Lett.* **89**, 255506 (2002).
- [12] L. E. Bove, F. Formiscano, F. Sacchetti, C. Petrillo, A. Ivanov, B. Dorner and F. Barocchi, *Phys. Rev. B* **71**, 014207 (2005).
- [13] F. J. Bermejo, and R. Fernandez-Perea, *Phys. Rev. E* **56**, 3358 (1997).
- [14] M. M. G. Alemany, J. Cases, C. Rey, L. E. Gonzales and L. J. Gallego, *Phys. Rev. E* **56**, 6818 (1997).
- [15] W. Gudowski, M. Dzugutov and K. E. Larsson, *Phys. Rev. E* **47**, 1693 (1993).
- [16] T. Scopigno, U. Balucani, G. Ruocco and F. Sette, *Phys. Rev. Lett.* **85**, 4076 (2000).
- [17] M. Canales, L. E. Gonzalez and J. A. Padro, *Phys. Rev. E* **50**, 3656 (1994).
- [18] U. Balucani, T. Torcini and R. Vallauri, *Phys. Rev. A* **46**, 2159 (1992).
- [19] U. Balucani, T. Torcini and R. Vallauri, *Phys. Rev. B* **47**, 3011 (1993).
- [20] S. K. Lai, L. Wang and M. P. Tosi *Phys. Rev. A* **42**, 7289 (1990).

- [21] J. A. Anta and A. A. Louis *Phys. Rev. B.* **61**, 11400 (2000).
- [22] H. S. Chen and S. K. Lai *Phys. Rev. A.* **45**, 3831 (1992).
- [23] F. Perron and G. Chabrier *Phys. Rev. A.* **43**, 2879 (1991).
- [24] M. Dzugutov *Phys. Rev. A.* **40**, 5434 (1989).
- [25] H. S. Kang, *Phys. Rev. B.* **60**, 6362 (1999).
- [26] J. F. Wax, N. Jakse and J. L. Bretonnet *Phys. Rev. B.* **55**, 12099 (1997).
- [27] K. K. Mon, *J. Chem. Phys.* **112**, 3245 (2000).
- [28] D. A. Young and F. J. Rogers, *J. Chem. Phys.* **81**, 2789 (1984).
- [29] N. F. Carnahan and K. E. Starling, *J. Chem. Phys.* **51**, 635 (1969).
- [30] L. Verlet and J. J. Weis *Phys. Rev. A.* **5**, 939 (1972).
- [31] K. K. Mon, *Phys. Rev. E.* **63**, 061203 (2001).
- [32] D. B. Amotz and G. Stell *J. Chem. Phys.* **119**, 10777 (2003).
- [33] D. B. Amotz and G. Stell *J. Chem. Phys.* **120**, 4844 (2004).
- [34] D. B. Amotz and G. Stell *J. Phys. Chem. B.* **108**, 6877 (2004).
- [35] M. Ross, H. E. DeWitt and W. B. Hubbard *Phys. Rev. A.* **24**, 1016 (1981).
- [36] K. K. Mon, R. Gann and D. Stroud *Phys. Rev. A.* **24**, 2145 (1981).

- [37] J. P. Hansen and D. Schiff *Mol. Phys.* **25**, 1281 (1973).
- [38] T. Scopigno, G. Ruocco, and F. Sette, *Rev. Mod. Phys.* **77**, 881 (2005).
- [39] Hansen J P and McDonald I R, *Theory of simple liquids* (New York: Academic, 1986).
- [40] Y. Waseda, *The Structure of Non-crystalline Materials, Liquids and Amorphous Solids* (McGraw-Hill, New York, 1980).
- [41] J. Hafner and G. Kahl, *J. Phys. F: Met. Phys.* **14**, 2259 (1984).
- [42] J. Hafner and W. Jank, *Phys. Rev. B.* **42**, 11530 (1990).
- [43] W. Jank and J. Hafner, *Phys. Rev. B.* **41**, 1497 (1990).
- [44] J. Hafner, *From Hamiltonians to Phase Diagrams* (Springer-Verlag, Berlin, 1987).
- [45] K. K. Mon, N. W. Ashcroft, and G. V. Chester, *Phys. Rev. B.* **19**, 5103 (1979).
- [46] de Gennes P G, *Physica.* **25**, 825 (1959).
- [47] T. Scopigno, R. Di Leonardo, L. Comez, A. Q. R. Baron, D. Fioretto, and G. Ruocco, *Phys. Rev. Lett.* **94**, 155301 (2005).
- [48] F. J. Bermejo, I. Bustinduy, S. J. Levett, J. W. Taylor, R. Fernández-Perea, and C. Cabrillo, *Phys. Rev. B* **72**, 104103 (2005).
- [49] U. Dahlborg and L. G. Olsson, *Phys. Rev. A.* **25**, 2712 (1982).

- [50] V. Hugouvieux, E. Farhi, M. R. Johnson, F. Juranyi, P. Bourges, and W. Kob, *Phys. Rev. B.* **75**, 104208 (2007).
- [51] G. Kresse and J. Hafner, *Phys. Rev. B.* **49**, 14251 (1994).
- [52] M. Dzugutov and U. Dahlborg, *Phys. Rev. A.* **40**, 4103 (1989).
- [53] S. Hosokawa, Y. Kawakita, W.-C. Pilgrim, and H. Sinn, *Phys. Rev. B.* **63**, 134205 (2001).
- [54] T. Itami, S. Munejiri, T. Masaki, H. Aoki, Y. Ishii, T. Kamiyama, Y. Senda, F. Shimojo and K. Hoshino, *Phys. Rev. B.* **67**, 064201 (2003).
- [55] S. Hosokawa, W.-C. Pilgrim, Y. Kawakita, K. Ohshima, S. Takeda, D. Ishikawa, S. Tsutsui, Y. Tanaka, and A. Q. R. Baron, *J. Phys.: Condens. Matter* **15**, L623 (2003).
- [56] E. G. D. Cohen, P. Westerhuijs, and I. M. de Schepper, *Phys. Rev. Lett.* **59**, 2872 (1987).
- [57] S. F. Tsay, *Phys. Rev. B.* **48**, 5945 (1993).
- [58] K. H. Tsai, T. M. Wu, S. F. Tsay, and T. J. Yang, *J. Phys.: Condens. Matter.* **19**, 205141 (2007).
- [59] S. F. Tsay and S. Wang, *Phys. Rev. B.* **50**, 108 (1994).
- [60] T. M. Wu, S. F. Tsay, S. L. Chang, and W. J. Ma, *Phys. Rev. B.* **64**, 064204 (2001).

- [61] J. R. D. Copley and S. W. Levesey, *Rep. Prog. Phys.* **38**, 461 (1975).
- [62] J. D. Honeycutt and H. C. Andersen, *J Phys. Chem.* **91**, 4950 (1987). By following the nomenclature in the reference, the atomic bonded pairs are characterized by four indices. The first index is 1 if the two atoms of an root pair is bonded. The second index represents the number of near-neighbors common and each bonded to the two atoms of the root pair. The third index gives the number of atomic bonds between the common neighbors. These three indices are not sufficient to characterize a diagram uniquely. Therefore, a fourth index is required to specify a unique correspondence between the arrangement of atomic bonds and diagrams.
- [63] S. F. Tsay *Phys. Rev. B.* **50**, 103 (1994).
- [64] I. M. de Schepper and E. G. D. Cohen, *Phys. Rev. A.* **22**, 287 (1980).
- [65] I. M. de Schepper, E. G. D. Cohen, and M. J. Zuilhof, *Phys. Lett. A.* **101**, 399 (1984).
- [66] N. Matsuda, K. Hoshino, and M. Watabe, *J. Chem. Phys.* **93**, 7350 (1990).
- [67] M. Canales and J. A. Padro, *Phys. Rev. E.* **56**, 1759 (1997).
- [68] C. Masciovecchio, G. Monaco, G. Ruocco, F. Sette, A. Cunsolo, M. Krisch, A. Mermet, M. Soltwisch and R. Verbeni, *Phys. Rev. Lett.* **80**, 544 (1998).
- [69] M. C. C. Ribeiro, M. Wilson, and P. A. Madden, *J. Chem. Phys.* **108**, 9027 (1998).

- [70] Y. S. Badyal, U. Bafle, K. Miyazaki, I. M. de Schepper, and W. Montfrooij, *Phys. Rev. E* **68**, 061208 (2003).
- [71] M. Patty, K. Schoen, and W. Montfrooij, *Phys. Rev. E* **73**, 021202 (2006).
- [72] J. A. Barker and D. Henderson, *Rev. Mod. Phys.* **48**, 587 (1976).
- [73] D. Chandler and J. D. Weeks, *Phys. Rev. Lett.* **25**, 149 (1970).
- [74] J. D. Weeks, D. Chandler, and H. C. Andersen, *J. Chem. Phys.* **54**, 5237 (1971).
- [75] H. C. Andersen, J. D. Weeks, and D. Chandler, *Phys. Rev. A.* **4**, 1597 (1971).
- [76] H. C. Andersen, D. Chandler, and J. D. Weeks, *Ann. Chem. Phys.* **34**, 105 (1976).
- [77] F. Lado, *Mol. Phys.* **52**, 871 (1984).
- [78] G. A. Mansoori and F. B. Canfield, *J. Chem. Phys.* **51**, 4958 (1969).
- [79] J. Rasaiah and G. Stell, *Mol. Phys.* **18**, 249 (1970).
- [80] D. Stroud and N. W. Ashcroft, *Phys. Rev. B.* **5**, 371 (1972).
- [81] J. Hafner, *Phys. Rev. A.* **16**, 351 (1977).
- [82] R. Kumaravadivel and R. Evans, *J. Phys. C.* **9**, 3877 (1977).
- [83] K. K. Mon, *J. Chem. Phys.* **115**, 4766 (2001).
- [84] K. K. Mon, *J. Chem. Phys.* **116**, 9392 (2002).

- [85] L. E. S. de Souza and D. Ben-Amotz, *Mol. Phys.* **78**, 137 (1993).
- [86] T. M. Wu, W. J. Ma, S. L. Chang, and S. F. Tsay, *Physica B.* **316-317**, 606 (2002).
- [87] Z. Yan, S. V. Buldyrev, N. Giovambattista, P. G. Debenedetti, and H. E. Stanley, *Phys. Rev. E.* **73**, 051204 (2005).
- [88] E. A. Jagla, *J. Chem. Phys.* **111**, 8980 (1999).
- [89] J. R. Errington and P. G. Debenedetti, *Nature.* **409**, 318 (2001).
- [90] R. Bellissent, C. Bergman, R. Ceolin and J. P. Gaspard *Phys. Rev. Lett.* **59**, 661 (1987).
- [91] J. Hafner *Phys. Rev. Lett.* **62**, 784 (1989).
- [92] L. Verlet and J. J. Weis *Molec. Phys.* **24**, 1013 (1972).

